J. Fluid Mech. (2002), *vol.* 450, *pp.* 343–375.
DOI: 10.1017/S0022112001006462 Printed in the United Kingdom

Aerodynamic flow-vectoring of a planar jet in a co-flowing stream

By DAVID W. LIM† AND LARRY G. REDEKOPP‡

Department of Aerospace and Mechanical Engineering,
University of Southern California, Los Angeles, CA 90089-1191, USA

(Received 14 December 1999 and in revised form 20 April 2001)

The vectoring of an incompressible, two-dimensional jet in a co-flowing stream is investigated by means of direct numerical simulation. The control input used to stimulate jet vectoring is accomplished through distributed suction from blunt-faced lips at the exit of the jet. The thrust vector methodology is based on suppression of global instabilities in the wake-shear layers formed between the co-flow and the jet. Once a critical suction volume flux needed to suppress these global instabilities is exceeded, local flow control can be realized through varying the distribution of suction across the base of the jet lips. It is found that the critical suction flux scales primarily with the ambient co-flow, not with the jet speed, and that lift-to-thrust ratios exceeding 15% can be realized. The effects of jet Reynolds number, jet-to-ambient velocity ratio, boundary-layer thickness, and geometric parameters on various performance characteristics are examined. It is also shown that the asymmetric flow control approach used for vectoring the jet can also be implemented in a symmetric configuration to enhance jet spreading. Significant increases in jet spreading can be realized when the symmetrically applied suction flux is sufficient to stimulate the sinuous mode of instability of the jet such that energetic flapping motion ensues.

1. Introduction

Broadly speaking, two types of flow control methodology have been employed to realize enhanced lift and manoeuvrability of aerodynamic vehicles. Extant methodologies can be classified as being either of mechanical or of aerodynamic type. Historically, mechanical flow-control devices, such as flaps and elevators, have been used extensively on aerodynamic surfaces to achieve lift augmentation and attitude control. The implementation of this class of movable (impermeable or perforated) control surfaces has matured considerably in recent years as actuators have been integrated into jet exhaust nozzles enabling a vectoring of the primary thrust for purposes of rapid manoeuvrability and post-stall performance (cf. Ashley 1995; North 1994). The incentives for super-manoeuvrability and the diminution of sharp edges and cross-sectional area have led to the incorporation of mechanical thrust vectoring technology as a standard option. The maturation of mechanical thrust vectoring technology has even led some to consider possible adaptations for commercial applications (cf. Proctor 1995). Nevertheless, there are certain penalties, as well as advantages, that

† Present address: Titan Research and Technology Division, 9410 Topanga Canyon Blvd. Suite 104, Chatsworth, CA 91311-5771, USA.
‡ Author to whom correspondence should be addressed.

accompany the use of these mechanical devices. Prominent penalties include, for example, added weight and mechanical complexity arising from incorporation of the necessary actuators into the airframe, limited fatigue life of thrust-vectored nozzles, relatively slow response time due to the inertia of the actuator system, and direct exposure of control surfaces to extreme temperatures.

A second class of flow control methodologies is that of aerodynamic or fluidic type. In this case, the control input is achieved entirely through spatial and temporal modification of boundary conditions along fixed, stationary surfaces. Fluidic controls are quite well-known, but only recently have they been pursued as a means of initiating and sustaining thrust vectoring. The realization of high lift or thrust vectoring control without the physical movement of any external aerodynamic surfaces offers promise for overcoming some of the prominent disadvantages of mechanical devices listed above. Development of this class of flow control approaches is, by comparison to that of mechanical devices, quite immature. So far, results in this class of approaches to aerodynamic flow vectoring of jets derive mostly from preliminary experiments, or rudimentary proof-of-concept studies, with only limited reporting of relevant fluid physics, even performance characteristics, in the open literature. Of course, vectoring through use of the Coanda effect is known (cf. Newman 1961), but the occurrence of free separation from, or only partial attachment to, the curved surface is quite sensitive to the radius of curvature and the size and speed of the jet. Practically, this technique is probably best-suited to small jets in the absence of co-flow. Several more recent approaches to jet vectoring are delineated below to contrast the underlying physical mechanisms that are exploited to realize a vectored response. As a general rule, all aerodynamic approaches to flow vectoring require some stimuli designed to induce a symmetry-breaking in a parallel streaming flow.

One approach to the vectoring of a planar supersonic jet involves the injection of a secondary stream through a line orifice on one side of the diverging section of the nozzle. As a consequence, a local separation of the jet flow is created with concomitant formation of an oblique shock upstream of the secondary injection line. The configuration is designed so that the oblique shock emanating from the separation line radiates just outside the exit on the opposite side of the nozzle and, thereby, serves to turn the primary jet flow across the entire plane of the oblique shock within the nozzle†. Turning angles approaching 15° have been reported, but these experiments involved only static tests (i.e. no co-flow).

Using an alternative approach, Strykowski, Krothapalli & Forliti (1996*a*) and Van der Veer & Strykowski (1997) pursued the vectoring of planar supersonic and subsonic jets, respectively, by the use of suction applied through an external collar surrounding the jet. The technique bears some relation to the Coanda effect, but with important distinctions that render the approach much more robust. When critical suction levels in the gap between the jet and the collar on one side are exceeded, they were able to produce vectoring of the jet to that side, reporting vectoring angles of up to 16° for supersonic jets. The deflection of the jet is attributed to the enhanced entrainment of the jet-shear layer on the suction side. More fundamentally, perhaps, the creation of a countercurrent mixing layer on the suction side can, as shown in separate studies by Strykowski & Wilcoxon (1993) and by Alvi *et al.* (1996), give rise to attendant onset of local absolute instability as a critical suction level is exceeded. This, in turn,

† Preliminary experiments using this approach are described in NASA TM 4575, Res. Tech. Highlights, Langley Research Center, 1993.

leads to an asymmetric entrainment and a preference for the jet to attach to the inner surface of the collar on the side with the largest entrainment.

This particular approach to jet vectoring has been carried forward in further work reported by Washington *et al.* (1996) and Alvi *et al.* (2000), proving its capability of providing proportional vectoring control and its use in multi-axis vectoring of either rectangular or circular jets. The technique has also been investigated for a supersonic jet immersed in an ambient, subsonic, co-flowing stream by Alvi & Strykowski (1999). The results generally show excellent promise for application to full-scale conditions.

In another promising approach to aerodynamic vectoring, Smith & Glezer (1997) and Smith (1999) have used piezoelectric actuators (plane strips) placed along the blunt-faced lips on both sides of a two-dimensional low-speed jet. The actuators operate without any net mass injection, creating a synthetic jet (i.e. an acoustic streaming flow) consisting entirely of entrained fluid (cf. Smith & Glezer 1998). This approach has obvious, very appealing advantages. The entrainment and rectified flows forced by the high-frequency pulsing of these actuators on a given side of the jet create local flow features which interact with the jet to deflect it toward the side where the actuators are excited. In studies to date, the jet issued into a stationary ambient and the effectiveness of the approach in the presence of co-flow has not been established.

The work described here differs from existing studies both in approach and in the basic flow configuration. We study the aerodynamic vectoring of a planar jet in a co-flowing stream through the application of distributed suction from the base of thin, blunt lips at the exit of the jet. The investigative approach relies entirely on numerical simulation. The methodology is an extension of the work of Hammond & Redekopp (1997*a*, *b*) and is based on principles of global instability and stimulated symmetry-breaking bifurcations of a streaming flow. Specifically, suction from the base region of the jet lips is used to suppress the existence of a global instability in the wakes of these blunt lips. Global instability in the (asymmetric) wake of a lip, manifested by synchronous vortex shedding, renders the flow quite insensitive to upstream 'control' perturbations. However, once the global instability is suppressed through suction, directional control of the parallel, streaming flow in the wake-shear layers formed downstream of the blunt lips and between the jet edges and the ambient stream can be achieved. This scenario was demonstrated by Hammond & Redekopp (1997*b*) and by Leu & Ho (2000) in the case of an isolated wake-shear layer. Hammond & Redekopp showed in particular that the distribution of suction flux across the base of the jet lips can be varied to achieve proportional directional control of the turning of the globally stabilized wake-shear layers. The extension of this result to the case of a jet in a co-flowing stream, which involves a coupled interaction between two wake-shear layers, is pursued in the present study.

2. Problem formulation

We consider a planar jet with width D and maximum velocity U_j immersed in a co-flowing stream with ambient speed U_∞. The lips of the jet consist of two plates forming blunt bases having thickness b aligned with the ambient, co-flowing stream. Each of the lips consists of two thin sheets of thickness ϵ with an interior flow region between them. The hollow cores of the two lips form a channel through which either a suction or blowing mass flux can be prescribed. The velocity profile at the base of each lip can be specified independently, forming the control inputs for jet vectoring. Both the jet flow and the ambient streams have boundary layers with respective thicknesses

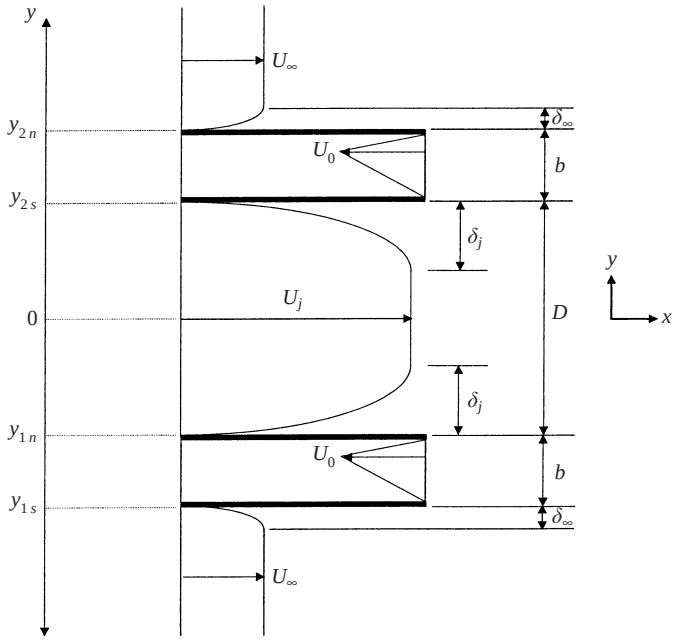

FIGURE 1. Flow configuration for the co-flowing jet problem.

δ_j and δ_∞ adjacent to the exterior sides of the plates forming the jet boundaries. The general flow configuration just described, together with the coordinate system employed in the analytical formulation, is shown schematically in figure 1.

Throughout the presentation, we choose to scale all flow and geometric variables in terms of the jet width D and the ambient speed U_∞. On this basis, the primary flow parameters for the problem are the Reynolds number $Re = U_\infty D/\nu$ and the jet velocity ratio $R = U_j/U_\infty$. The jet Reynolds number Re_j is determined directly by these parameters, being given by the product $Re\ R$. Although the variables defined in figure 1 are dimensional, the discussion which follows will employ many of the same symbols for the relevant geometric parameters with the understanding that these variables are scaled appropriately in terms of D. In particular, we have the base thickness b and boundary-layer thicknesses δ_j and δ_∞, which together with the coordinates (x, y), are henceforth dimensionless variables being scaled with D.

In addition to these parameters we must define a control parameter characterizing the suction/blowing applied at the base of each of the jet lips. In this study, we focus exclusively on the case of base suction and employ, for computational and physical simplicity, a base-suction velocity profile composed of linearly varying segments. The dimensionless suction profile $U_s(y)$ is defined in terms of the cross-channel coordinate ξ as shown in figure 2 with ξ_0 and U_0 specifying the location and value of the peak suction velocity. As shown by Hammond & Redekopp (1997*b*), a key control parameter affecting the vectoring of an individual wake-shear layer is the lateral position of the 'centre of flux' for the suction. Practically, we might vary the distribution of flux by applying uniform suction through either the upper or lower half of a jet lip, but for computational purposes it is advantageous to avoid infinite velocity gradients at a wall corner. In an attempt to limit the extent of the parameter space of the problem, but yet to accentuate the asymmetry of the suction profile, the position of the peak suction velocity is always set at $\xi_0 = \frac{4}{5}b$. The control parameter

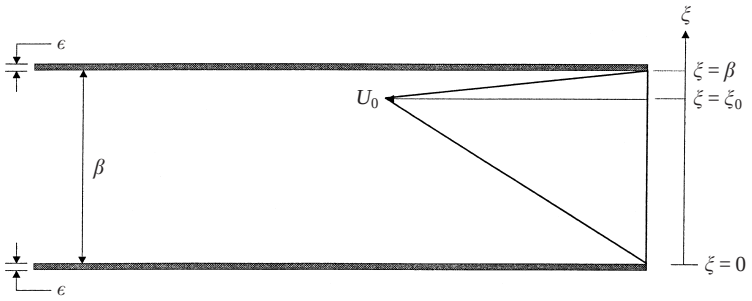

FIGURE 2. Nozzle exit and suction profile.

we use is the suction volume flux q defined by

$$q = \frac{1}{b}\int U_s(y)\,\mathrm{d}y.$$

The objective of the study reported here is to elucidate the role of the various parameters defined above on the lift characteristics of the co-flowing jet configuration.

The field equations for the problem are the Navier–Stokes equations for an incompressible fluid in planar motion:

$$\frac{\partial u}{\partial x} + \frac{\partial v}{\partial y} = 0, \tag{2.1}$$

$$\frac{\partial u}{\partial t} + u\frac{\partial u}{\partial x} + v\frac{\partial u}{\partial y} = -\frac{\partial p}{\partial x} + \frac{1}{Re}\left(\frac{\partial^2 u}{\partial x^2} + \frac{\partial^2 u}{\partial y^2}\right), \tag{2.2}$$

$$\frac{\partial v}{\partial t} + u\frac{\partial v}{\partial x} + v\frac{\partial v}{\partial y} = -\frac{\partial p}{\partial y} + \frac{1}{Re}\left(\frac{\partial^2 v}{\partial x^2} + \frac{\partial^2 v}{\partial y^2}\right). \tag{2.3}$$

The inlet flow is prescribed along a plane positioned one jet-width upstream of the jet exit, with boundary-layer profiles at this inlet plane taken to be quadratically varying functions of the transverse coordinate. No-slip conditions are applied along the impermeable boundaries of the jet, and the prescribed (normal) suction velocity is applied along the base of the jet lips. The use of a suction profile with vanishing velocity at the inside edges of the suction channel avoided extreme gradients at the tips of the trailing edge. When there was no applied suction, the no-slip condition was imposed along the blunt edges of the jet lips. In either case, however, implementation of the numerical simulation of the flow around the sharp corners at the trailing edges of the blunt lips required special treatment. The modelling of the flow in the vicinity of these corners, as well as discussion of the far-field boundary conditions, is described in conjunction with the numerical scheme in the next section.

3. Computational methodology

3.1. *Numerical scheme*

The two-dimensional, incompressible Navier–Stokes equations are solved in their primitive variable form using the two-dimensional version of the QUICKEST scheme (Leonard 1979) as formulated by Davis & Moore (1982). Davis & Moore applied this quadratic upwind scheme in their numerical studies of various open and confined shear flows, and later Hammond & Redekopp adopted it in their study of wake flow

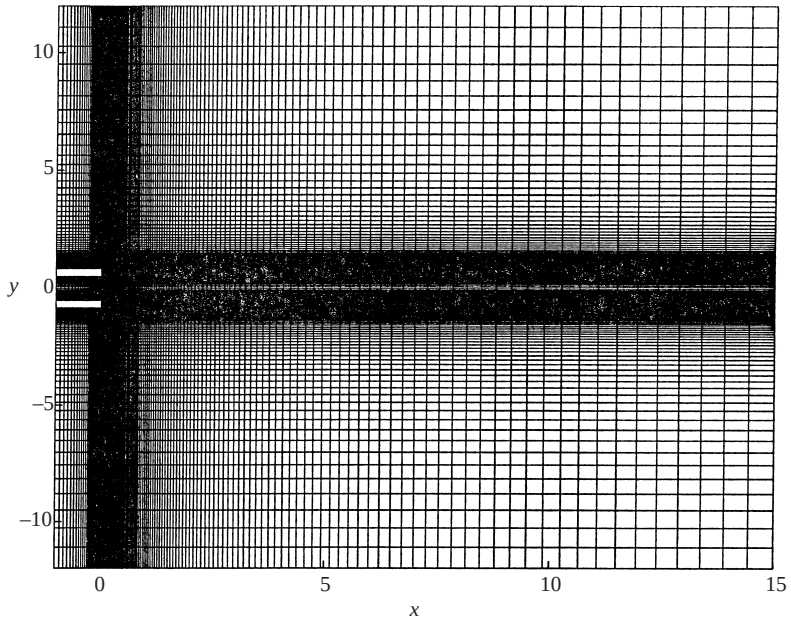

FIGURE 3. Medium grid used for production work.

vectoring. When diffusion terms are small, the two-dimensional QUICKEST scheme attains third-order accuracy in space and second-order accuracy in time; otherwise, the scheme is second-order accurate in space and first-order in time. The main advantage of using the QUICKEST scheme is that it has excellent stability properties without the undesirable (and mostly unacceptable) artificial diffusion problems associated with first-order upwind schemes. The CFL condition suffices for numerical stability (Leonard 1979; Davis & Moore 1982).

In discretizing the governing equations, the projection method (Chorin 1968) is used to decouple the continuity equation from the momentum equations and, as a result, a Poisson equation for pressure is solved in place of the continuity equation to satisfy the conservation of mass. The Poisson equation is solved iteratively using the successive line over-relaxation method, with an optimal over-relaxation value of $\lambda_{opt} = 1.7$, which was obtained by a simple convergence test (see, for example, Ferziger & Perić 1996).

The discretized equations were solved on a rectangular, staggered grid in which the pressure was defined at cell centres and the velocities at cell faces. Variable grid spacing enabled concentration of mesh points near solid surfaces, and a systematic grid refinement test was necessary to ensure that the production version mesh would adequately resolve the flow field at all levels of suction for the study. The upper and lower boundaries of the computational domain were set at $y = 12.0$ to uphold approximately uniform flow conditions along these boundaries. The mesh used for the production work had 156 cells in the streamwise direction and 216 cells in the cross-stream direction, and is shown in figure 3.

3.2. *Boundary conditions*

At the inlet as well as at the suction base (when suction was present), user-defined velocity profiles were assigned as discussed previously and these were held fixed in time for each simulation. The no-slip condition was imposed on all impermeable solid

surfaces. However, ambiguity existed at the points corresponding to the corners of the trailing edges since, in the control volume formulation of the momentum equations, half of the cell face adjacent to these corner points fell on the solid surface while the other half experienced convective flux. Non-zero velocities had to be allowed at these points and were obtained by requiring zero divergence for the control volume.

At the open boundary at the downstream end of the computational domain, the flow was expected to be unsteady, but the exact nature of the flow was unknown. A main goal of the boundary condition at this location is to allow the passage of vortical structures without causing numerical distortion or feedback (Buell & Huerre 1988). The boundary condition that was employed for this purpose was one that has gained some popularity in recent years, namely the one-dimensional linear convection equation (see, for example, Ferziger & Perić 1996; Maekawa, Mansour & Buell 1992; Pauley, Moin & Reynolds 1990; Salvetti, Orlandi & Yerzicco 1996) given by:

$$\frac{\partial u}{\partial t} + U_a \frac{\partial u}{\partial x} = 0, \tag{3.1}$$

$$\frac{\partial v}{\partial t} + U_a \frac{\partial v}{\partial x} = 0. \tag{3.2}$$

In equations (3.1) and (3.2), the advection velocity U_a is held constant at some representative value. Maekawa *et al.* (1992) reported that the actual value of the constant did not make much difference in the results of their simulation of two-dimensional wake flows. Three different values of U_a were tested for the present study: the jet velocity U_j, a spatially averaged inlet velocity U_{avg}, and the mean velocity between U_j and U_∞, i.e. $U_{1/2} = \frac{1}{2}(U_j + U_\infty)$. It was found that changing the value of U_a had a quite limited influence in the immediate vicinity of the downstream exit of the domain. However, in view of the present objectives, it made no discernable difference in the near-field solution. In general, U_a was set equal to $U_{1/2}$.

The upper and lower boundaries of the computational domain were placed sufficiently far away from the jet so as to assign a near free-stream condition at these boundaries. Setting $y_{max} = 12.0$ proved to be sufficient for this purpose, as comparison of local and global flow properties with $y_{max} = 18.0$ showed essentially no difference. Along these boundaries, the horizontal velocity was fixed at the uniform ambient condition while the vertical gradient of the cross-stream velocity was made to vanish, allowing for some vertical momentum flux across the boundary.

For the pressure, Peyret & Taylor (1983) have shown that the projection method allows the homogeneous Neumann condition to be applied at all boundaries where the normal velocity at the next time step is known. Accordingly, at the inlet and the downstream exit of the domain, as well as at all solid surfaces, the pressure boundary condition was given by zero normal gradient. At the upper and lower boundaries of the domain, where the gradient of the normal velocity was made to vanish, a Dirichlet condition with zero pressure was assigned. Note that the particular value of the pressure at these boundaries was immaterial since the pressure appears only as a derivative term.

4. Results and discussion

4.1. *Instability of the vectored flow*

Figure 4 shows an instantaneous velocity field of the unstable jet at $Re_j = 1000$ when there is no suction. The blacker regions in the flow field are an artefact of

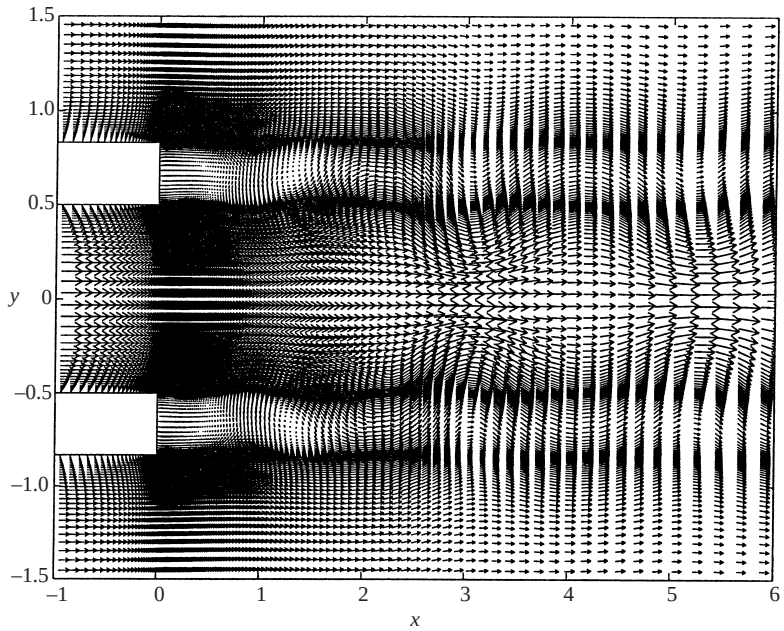

FIGURE 4. Vector field of co-flowing jet without suction, $Re = 1000$, $R = 2$.

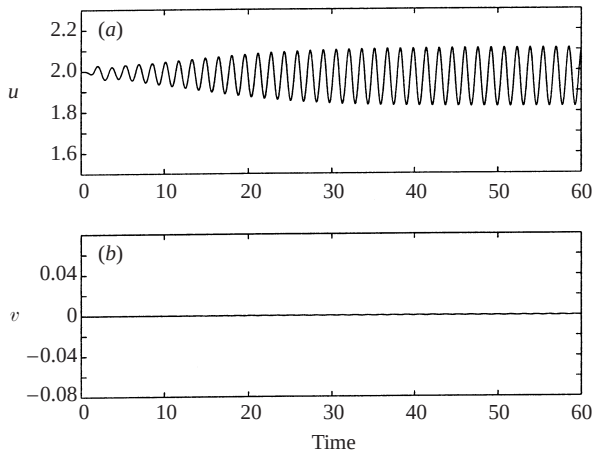

FIGURE 5. Time history of the velocity components of co-flowing jet without suction, $x = 1.0$, $y = 0$, $Re_j = 1000$ and $R = 2$.

the concentration of grid points and should not be confused as streamline patterns. The vector plot reveals that the mode of instability is of varicose type, a fact further illuminated by figure 5 which shows the time-history of the velocity components at a point located one jet-width downstream of the jet exit along the centreline of the jet. It should be noted that since homogeneous, co-flowing jets are convectively unstable (namely in the limiting case of infinitely thin, stress-free plates) they are unable to sustain instability without continual forcing. On the other hand, the regular, self-sustained oscillations exhibited here are a manifestation of a global mode associated with the wake-shear layers that form behind the plates; that is, the absolute instability in the near-wake regions enables the intrinsic jet dynamics that is observed.

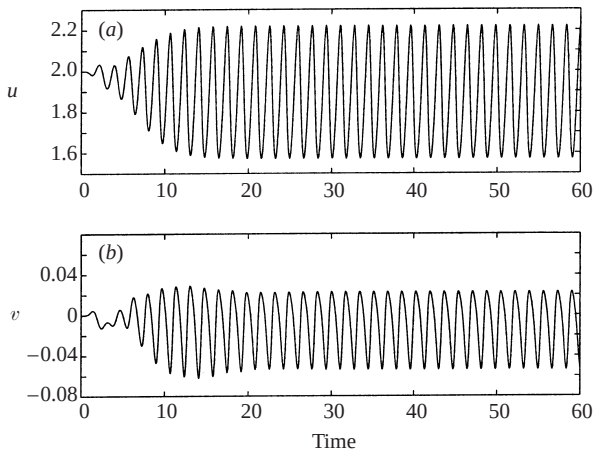

FIGURE 6. Time history of the velocity components of co-flowing jet with suction, $x = 1.0$, $y = 0$, $U_0 = 0.3$, $Re_j = 1000$ and $R = 2$.

The data shown in figure 5 also reveal the inherent quality of the simulation. The cross-stream velocity for a pure varicose mode should vanish along the centreline (line of symmetry) of the jet. This is satisfied to less than 10^{-3} for times in excess of ten periods of oscillation in the saturated state of global instability. The almost imperceptible level of oscillation for the varicose mode in figure 5(b) should be compared with the prominent amplitude of the cross-stream velocity variations for the sinuous mode shown in figure 6(b). The results shown in these figures provide a measure of the accuracy and consistency of the simulation algorithm.

When asymmetric suction is introduced at the jet nozzle (distribution shown in figures 1 and 2), the perturbation to the overall symmetry of the velocity profile stimulates the sinuous mode of instability of the jet and, with sufficient suction, the jet flow switches to a flapping motion. The changed mode of instability can be inferred from figure 6 which shows the time history of the velocity components for a relatively small suction velocity of $U_0 = 0.3$. Note that the same scales were employed in figures 5 and 6 for comparison purposes. The cross-stream component now shows significant oscillations along the centreline owing to the flapping motion of the jet. It is also evident that the oscillations take place about a negative mean velocity. That is, there is an average vectoring effect such that the flapping motion takes place about a small downward angle from the jet exit.

Further increase in suction gives rise to a more pronounced flapping motion of the jet at first, but at a critical suction level, which for the benchmark case of $Re_j = 1000$ was approximately $U_0 = 0.7$ ($q = 0.07$), the fluctuations associated with the flow instability are abruptly and drastically reduced, and the jet experiences an almost steady vectoring effect. The trend is illustrated in figures 7 and 8 which show, respectively, the instantaneous vector fields at a subcritical suction velocity of $U_0 = 0.6$ and at a supercritical suction velocity of $U_0 = 0.8$. We can immediately observe that while flapping motion is very energetic for the subcritical suction case, the jet is vectored quite steadily in the supercritical case. By contrast, the flapping motion is drastically reduced for supercritical suction and the velocity profile at $x = 6$ in figure 8 is decidedly asymmetric (i.e. has a peak streamwise velocity below the centreline). The shift in the mean streamwise velocity profile for the vectored jet is shown in more detail in figure 9.

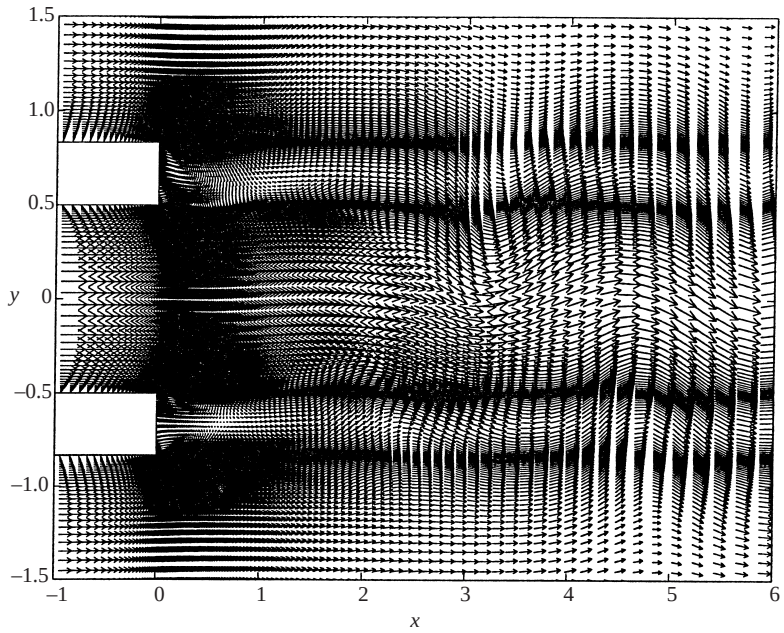

FIGURE 7. Instantaneous velocity field at moderately high suction, $U_0 = 0.6$, $Re_j = 1000$ and $R = 2$.

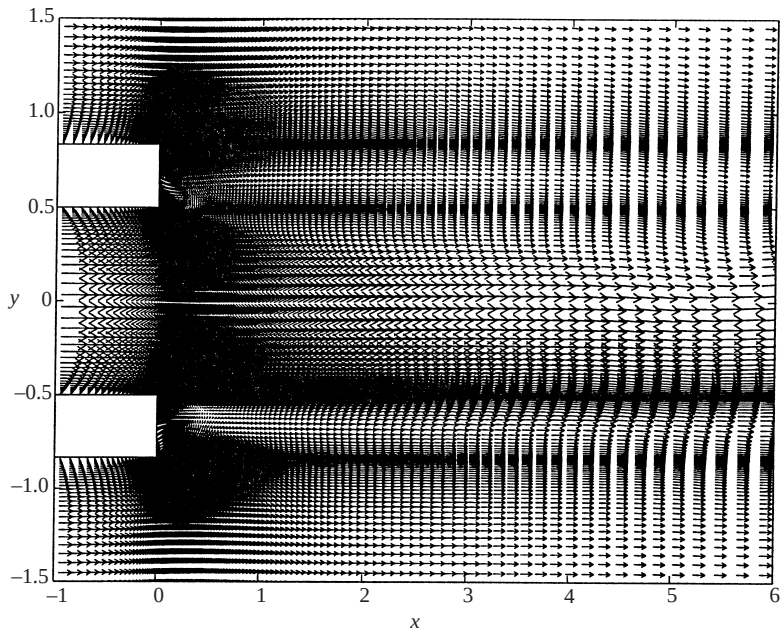

FIGURE 8. Instantaneous velocity field at moderately high suction, $U_0 = 0.8$, $Re_j = 1000$ and $R = 2$.

The existence of a critical suction velocity prior to the onset of a substantial vectoring effect is reminiscent of the wake vectoring results obtained by Hammond & Redekopp (1997*b*), in which a critical suction level marked the point of effective flow vectoring control. They, as well as Leu & Ho (2000), showed by concomitant instability calculations that the onset of flow vectoring coincided with the suppression of global

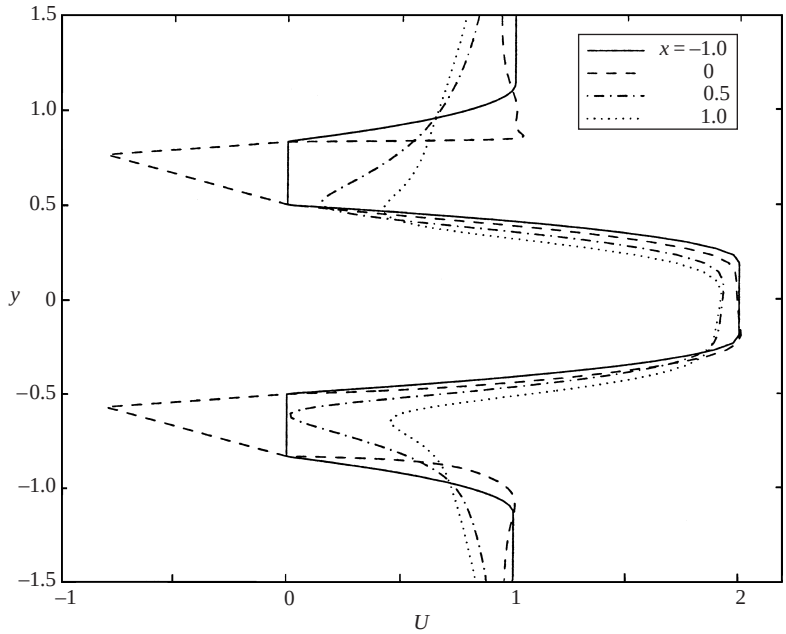

FIGURE 9. Instantaneous co-flowing jet profile at various locations of x for vectored case, $Re = 1000$, $R = 2$ and $U_0 = 0.8$.

instability in the wake-shear layer. Indeed, the drastic reduction in the magnitude of oscillations associated with the vectoring effect in the present study lends itself to a similar interpretation, even though a complete suppression of global instability was not observed in this case. The reason for the persistence of synchronous dynamics at supercritical suction levels in the present case of the co-flowing jet is not clear. The coupling of the neighbouring wake-shear layers presents a serious challenge in identifying the exact source of the persistent oscillations. There are probably a spectrum of global modes for the jet formed by the high-speed flow between two wake-shear layers, and simulation of the fully nonlinear dynamics need not necessarily lock onto a single nonlinear mode. Nevertheless, the dynamics in all cases examined in this study are characterized by a single dominant frequency, a result which we interpret as the gravest mode of the jet. Yet, evidence indicates that a significant vectoring effect, emerging rather abruptly past the critical suction level, just as in the configuration studied by Hammond & Redekopp (1997*b*), can be achieved apparently without the suppression of the entire spectrum of global modes in the flow.

It is perhaps worth noting that when the Reynolds number was increased to $Re_j = 1500$ at a supercritical suction velocity of $U_0 = 0.8$, the periodic oscillations in the flow field became even more energetic than those observed in the $Re_j = 1000$ case, while the vectoring effect was noticeably stronger in the mean. Further discussion of the global mode dynamics will be provided in § 5 in the context of the lift characteristics of the vectored flow.

4.2. *Entrainment patterns*

As discussed by Hammond & Redekopp (1997*b*), flow vectoring implies the application or inducement of a localized force which breaks the symmetry inherent in streaming flows. A close examination of the flow entrainment patterns provides a

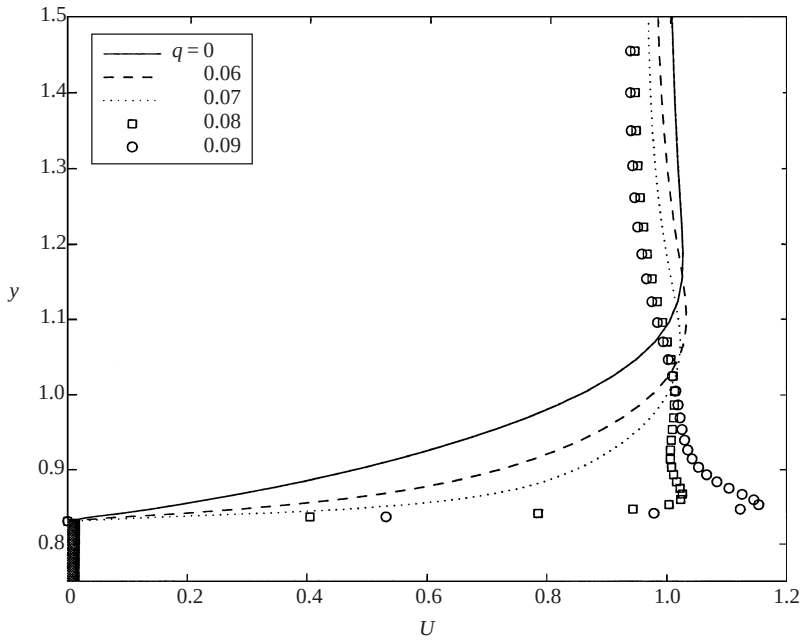

FIGURE 10. Instantaneous co-flow boundary-layer profiles at $x = -0.0025$ on the upper plate surface, for various values of suction flux ratio, $Re_j = 1000$, $b = \frac{1}{3}$ and $R = 2$.

valuable insight into the mechanism of momentum transfer. The details of the flow near the trailing edges indicate that when suction is applied, fluid from the adjacent boundary layers is quickly entrained into the wake region behind each plate. Figure 9 shows instantaneous streamwise velocity profiles of the co-flowing jet when a super-critical suction of $U_0 = 0.8$ ($q = 0.082$) was applied. Profiles were captured at four different streamwise locations, namely $x = -1.0$, 0, 0.5 and 1.0, after the oscillations became saturated and at the instant when the streamwise velocity at $x = 1.0$ and $y = 0$ reached its peak. Note that the solid profile corresponding to the inlet ($x = -1.0$) provides the base state for comparison, while the dashed profile corresponding to the nozzle exit ($x = 0$) shows the distribution of suction.

Examination of the dashed profile ($x = 0$), reveals that the boundary layers on the low-speed side of either plate (i.e. the boundary layers in the ambient co-flow side) show a greater tendency towards entrainment than the boundary layers of the high-speed side (i.e. the jet side). Of the two co-flow boundary layers, the upper boundary layer has a much sharper profile near the plate surface, indicating a stronger response to suction owing to its proximity to the point of maximum suction velocity. It also has a lower momentum and responds more readily to transverse pressure gradients.

Between the nozzle exit and $x = 1.0$, the co-flowing jet profile undergoes a more far-reaching change. No backflow is observed beyond $x = 0.5$, and the deficit regions between the jet and the co-flow are substantially filled in by the entrained fluid from the boundary layers. Moreover, fluid is drawn from the outer regions of the co-flow, greatly increasing the vertical extent of the shear region. The strong entrainment of the upper co-flow boundary layer stands in sharp contrast to the weak response from the upper jet shear layer, which is only slightly pushed downward, presumably owing to the influence of suction in the lower plate. Near the lower plate, the entrainment from the lower jet shear layer and that from the co-flow are in competition with each

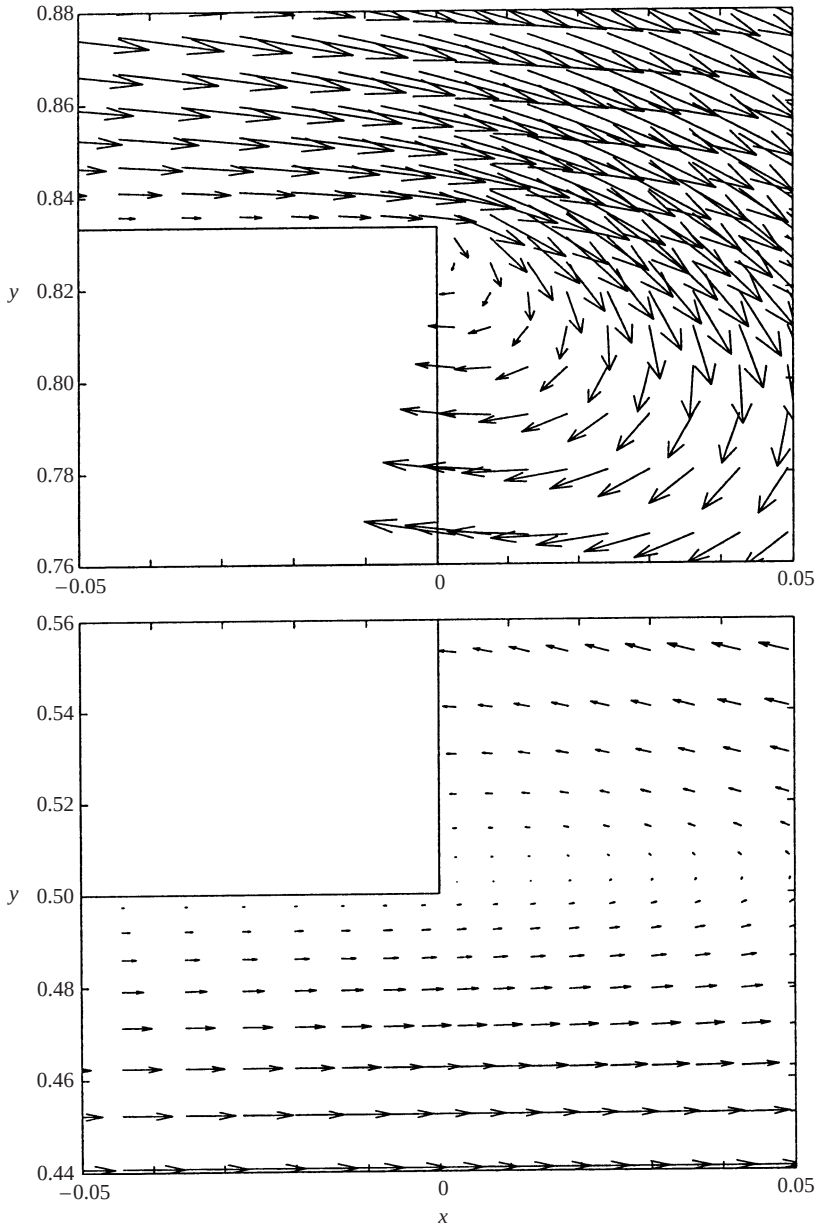

FIGURE 11. Instantaneous velocity vector fields near the upper and lower corners of the upper plate trailing edge, $Re = 1000$, $R = 2$ and $U_0 = 0.8$.

other, since the point of maximum suction velocity is closer to the high-speed side this time and induces a significant response from the lower jet shear layer. The net effect of the asymmetric entrainment pattern is to push the entire jet downward, as is evident from the dotted profile at $x = 1.0$.

Figure 10 focuses on the upper co-flow boundary layer and shows the streamwise velocity profiles immediately upstream ($x = -0.0025$) of separation for five different values of the suction flux ratio, varying from $q = 0$ to $q = 0.09$. Again, all profiles were taken at the same phase of jet oscillations. Clearly, increasing suction increases

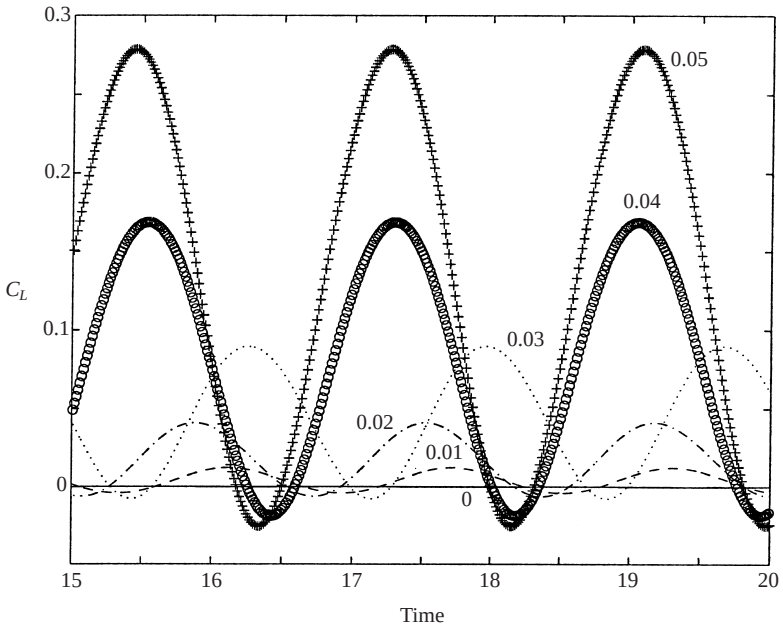

FIGURE 12. Time-dependent lift produced at various suction levels, $Re = 1000$ and $R = 2$. (The numbers next to curves indicate the value of the suction flux ratio q.)

the tendency of the boundary-layer to be entrained, but it is interesting to note that the boundary-layer profile remains essentially similar for $q = 0$ to $q = 0.07$. However, between $q = 0.07$ and $q = 0.08$, approximately corresponding to the critical suction flux ratio, a radical change occurs in the boundary-layer profile whereby a 'wall jet' formation takes place for $q = 0.08$. This suggests that the influence of suction is acutely felt by the boundary-layer when the suction flux ratio exceeds $q = 0.07$, in apparent agreement with the abrupt increase in vectoring effect that was observed earlier.

Finally, figure 11 shows the vector field plot for the same case, zoomed near the trailing edge of the upper plate. The upper and lower figures correspond, respectively, to the top and bottom corners of that trailing edge. In each figure, the horizontal and vertical dimensions span 10% and 12% of the jet width, respectively. Clearly, the asymmetry that was already present in the wake of the trailing edge (i.e. low-speed flow in the upper streams and high-speed flow in the lower streams) is efficiently exploited by the asymmetric suction profile.

4.3. *Lift characteristics*

One way to quantify the effect of flow vectoring is to compute the lift per unit span produced by the vectored fluid. The lift force was computed by using the integral form of the momentum equation applied to a control volume extending in the streamwise direction from the inlet to a distance several jet widths downstream of the jet exit. The cross-stream extent of the control volume was positioned symmetrically with respect to the jet centreline and extending at least two jet widths on either side. Computed values of the lift force were shown to be quite insensitive to variations in the boundaries of the control volume so long as the lateral and downstream boundaries were not too close to the jet exit. Early work by Hammond & Redekopp (1997*b*) using the same integration scheme showed that this approach yielded values

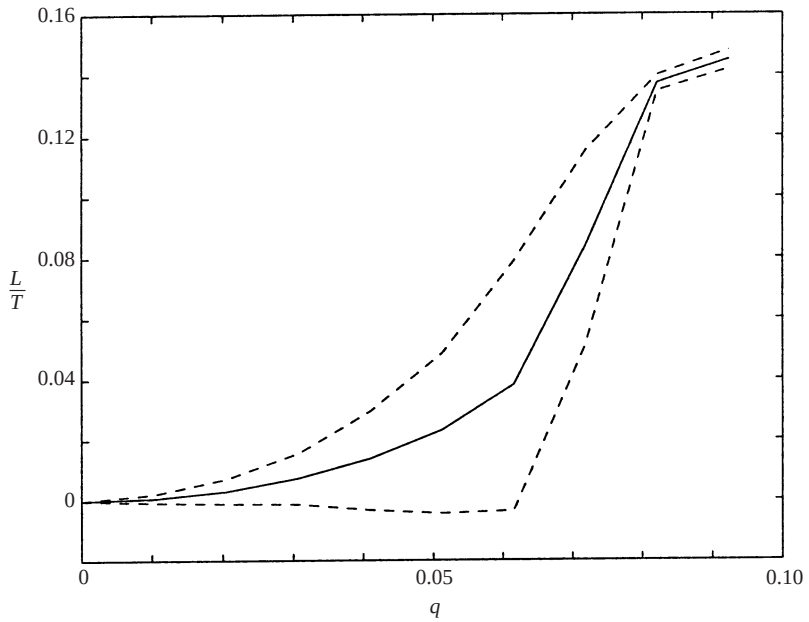

FIGURE 13. ——, Time-averaged lift-to-thrust ratio and - - -, the corresponding maximum and minimum at $Re = 1000$ and $R = 2$.

of the lift which were in good agreement with the integration of the pressure around the jet lips.

Figure 12 shows the time-dependent lift coefficient for six different values of maximum suction velocity at $Re_j = 1000$, sampled after the oscillations reached a saturated state. The lift coefficient C_L is defined as

$$C_L = \frac{L}{\frac{1}{2}\rho U_\infty^2 D}. \tag{4.1}$$

As suction is increased from $q = 0$ to $q = 0.05$, the maximum value of C_L continues to rise, reaching $C_L = 0.28$ at $q = 0.05$, while the minimum C_L is held above a value of -0.03 for all suction levels shown. We comment that the computation of non-zero values of C_L implies that a turning of the jet has occurred prior to the jet exit. Although this is not entirely obvious in figure 11, it is a necessary consequence of the momentum theorem applied here.

The time-averaged lift characteristics for the same set of simulations are presented in figure 13. The solid curve corresponds to the time-averaged lift-to-thrust ratio L/T while the dotted curves define the upper and lower limits of L/T in the time-dependent solution. Consistent with the observations made in the previous sections, the effect of suction on the lift is quite marginal for small levels of suction, but when the suction flux ratio reaches about $q = 0.07$, there is a sudden increase in the lift and the ratio L/T quickly reaches a value of about 15% at $q = 0.08$.

As discussed earlier, the fairly steep rise in the vectoring response curve when the critical suction level is exceeded seems to imply a fairly sudden suppression, or at least a sufficient weakening, of the global instabilities that in general make a streaming flow quite 'stiff'. Whereas a complete suppression of global instability was not observed in the present study, the persisting oscillations in the supercritical regime were clearly weaker than the oscillations observed in the subcritical suction range. Based on the

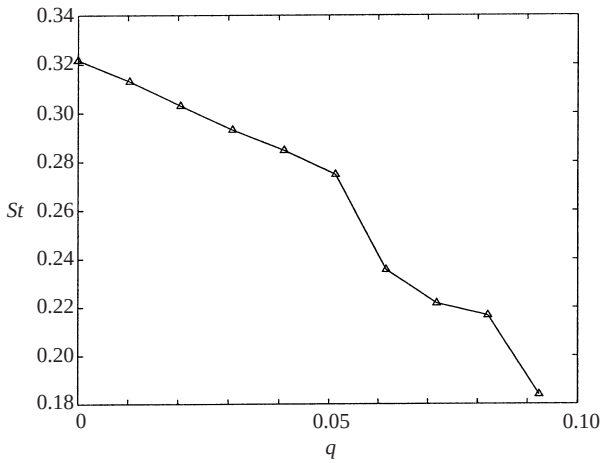

FIGURE 14. Effect of suction flux ratio on the Strouhal number, $Re = 1000$ and $R = 2$.

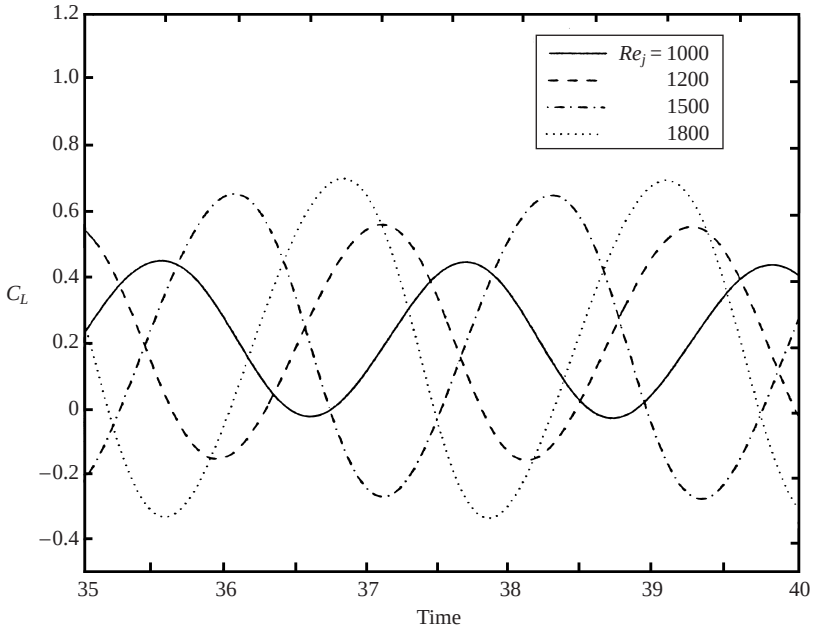

FIGURE 15. Time-history of C_L at various values of Re_j, $U_0 = 0.6$, $b = \frac{1}{3}$ and $R = 2$.

results of Hammond & Redekopp (1997*b*), it is conjectured that the global instability of the individual wakes is suppressed once the suction velocity U_0 exceeds a critical level, thereby enabling the local turning of each wake. However, the global instability of the coupled wakes (i.e. the jet) may not be completely suppressed by the present use of suction, and this may explain the persisting instability in the flow even as the jet is vectored significantly. The variation of the Strouhal number with suction flux as shown in figure 14, revealing different slopes before and after the vectoring transition, suggests a change in the dynamical character of the vectored flow before and after the transition.

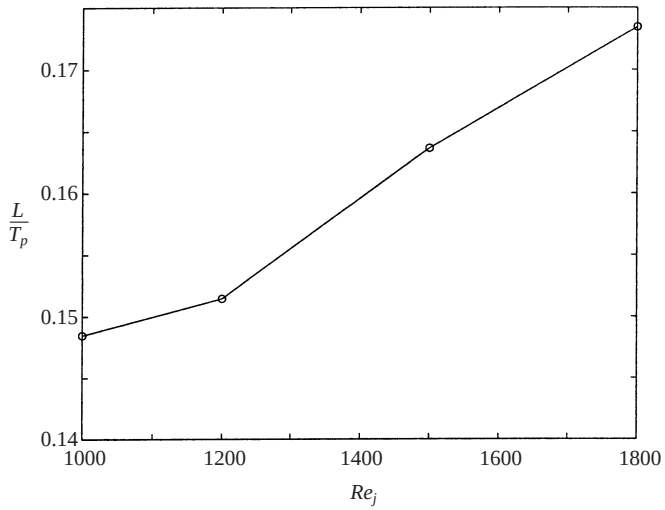

FIGURE 16. Peak value of time-averaged lift-to-thrust ratio as a function of the jet Reynolds number, $b = \frac{1}{3}$ and $R = 2$.

4.3.1. *Effect of Reynolds number*

The Reynolds number was varied from 1000 to 1800 for the benchmark case. Figure 15 shows the time history of C_L for four different values of the Reynolds number at a fixed value $U_0 = 0.6$ of the suction velocity. The oscillatory behaviour shown is for the saturated state after initial transients have decayed. The chief effect of varying the Reynolds number was that the oscillations became more energetic as the Reynolds number was increased. In fact, going from 1000 to 1800, the amplitude of oscillations in the lift increased approximately by a factor of two while the time-averaged lift showed a relatively small variation. When the time-averaged lift curves for the four different values of the Reynolds number were compared, it was found that all of them were essentially identical in the subcritical suction region, and that a small increase takes place in the supercritical region with increasing Reynolds number. From 1000 to 1800, there was about a 17% increase in the maximum average lift attained within the range of suction for this study. The peak average lift-to-thrust ratio increased from about 0.148 to 0.173 as shown in figure 16, but it is also clear that there is a positive slope indicating a growing lift-to-thrust ratio with increasing jet Reynolds number.

4.3.2. *Effect of velocity ratio*

Three different values of the velocity ratio, namely $R = 2.0$, 2.5 and 3.0, were tested to examine its effect on vectoring. From a simple momentum consideration, it would seem intuitive that more effort is needed to vector the high-speed flow as the velocity of the jet increases relative to the co-flow. This was confirmed in one sense, but not in another. The distinction arises because two separate quantities must be considered in evaluating the effectiveness of vectoring. One is the critical suction (i.e. control input) which is indicative of the amount of energy that must be put into the system to achieve a meaningful vectoring effect. The other is the maximum lift (i.e. response), indicating the useful output. A primary objective of flow vectoring would be to minimize the former while maximizing the latter.

Figure 17 shows the time-averaged lift curves for three different values of the

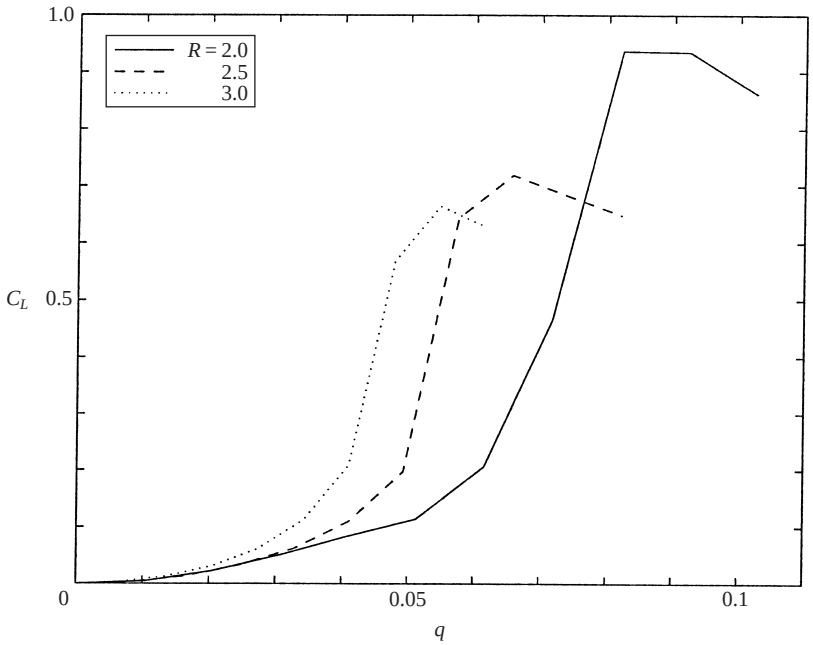

FIGURE 17. Time-averaged lift at various values of velocity ratio, $Re_j = 1500$ and $b = \frac{1}{3}$.

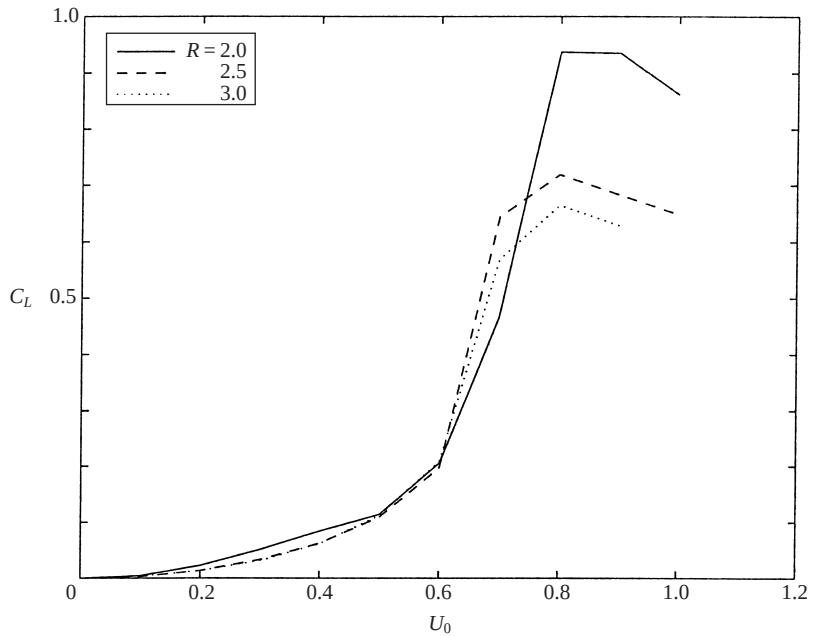

FIGURE 18. Time-averaged lift coefficient as a function of U_0 at various values of velocity ratio, $Re_j = 1500$ and $b = \frac{1}{3}$.

velocity ratio at a Reynolds number of 1500. As the velocity ratio is increased, the jet is vectored at lower values of the suction flux ratio. In fact, the critical suction flux ratio is reduced by approximately 40% (from 0.07 to 0.04) as the velocity ratio increases from 2 to 3. This can be misleading, however, since the suction flux ratio at

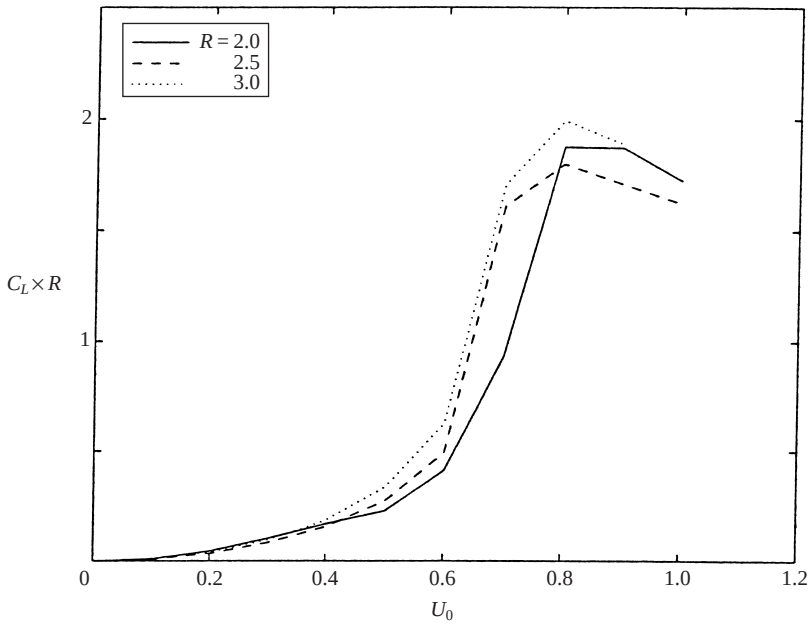

FIGURE 19. Scaled time-averaged lift coefficient as a function of U_0 at various values of velocity ratio, $Re_j = 1500$ and $b = \frac{1}{3}$.

any given suction velocity decreases as the jet velocity is increased. In fact, when the abscissa in figure 17 is replaced by the maximum suction velocity, the three curves collapse in the subcritical region as shown in figure 18, and the differences in the critical suction velocity become marginal. This shows that approximately the same amount of suction is required to initiate jet vectoring regardless of the velocity ratio. Moreover, it is clear that the maximum lift is obtained for the lowest velocity ratio. Accordingly, jets with lower velocity ratios are more effectively vectored than those with higher values of R. Indeed, the maximum lift scales directly with the reciprocal of the velocity ratio, a result shown decisively in figure 19.

4.3.3. *Effect of geometry*

Another parameter of interest for the vectoring study was the relative plate thickness ratio b. It is likely in real applications that the ratio b would be smaller than the benchmark case. Hence, a value of $b = \frac{1}{4}$ was tested against the benchmark case of $b = \frac{1}{3}$. In terms of wake-shear layers, the reduction in b can be thought of as further separating the two wake-shear layers so that the coupling between them is made weaker. This point is easily seen by considering the plate thickness as the length scale for each wake-shear layer.

Computationally, the change in the plate thickness b did not affect the thickness ϵ of the sheets that form the plate, since the minimum grid spacing was held at the same level as before. The maximum suction velocity was applied using the same formulation (i.e. the maximum positioned $\frac{4}{5}$ of the way up from the bottom surface of each plate). Of course, at the same maximum suction velocity, the total suction flux was proportionally decreased for the $b = \frac{1}{4}$ case. Figure 20 shows the time-averaged lift coefficient as a function of the suction flux ratio for the two different values of b. Clearly, a smaller suction flux ratio is needed to vector the jet when $b = \frac{1}{4}$. However, when the averaged lift coefficient is plotted against the maximum suction velocity, as

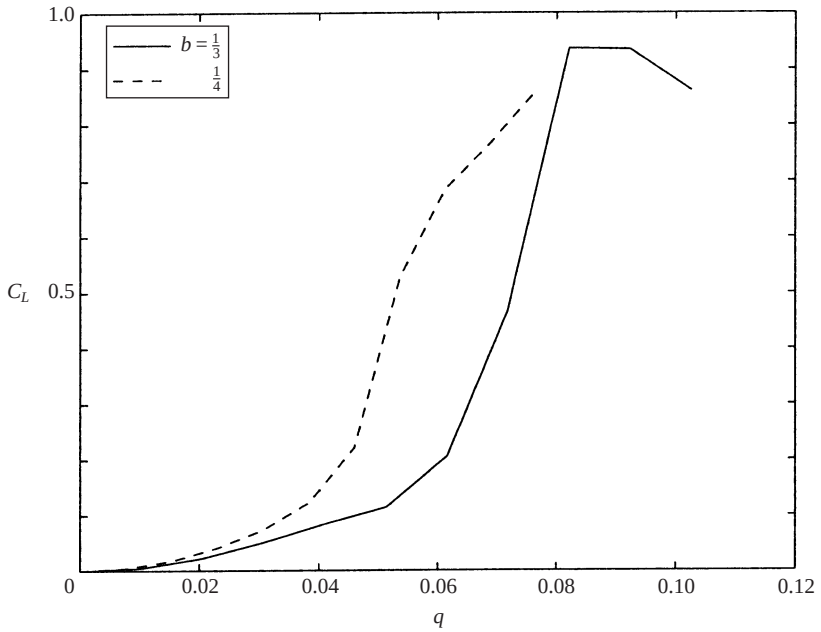

FIGURE 20. Coefficient of lift at $Re_j = 1000$ and $R = 2$.

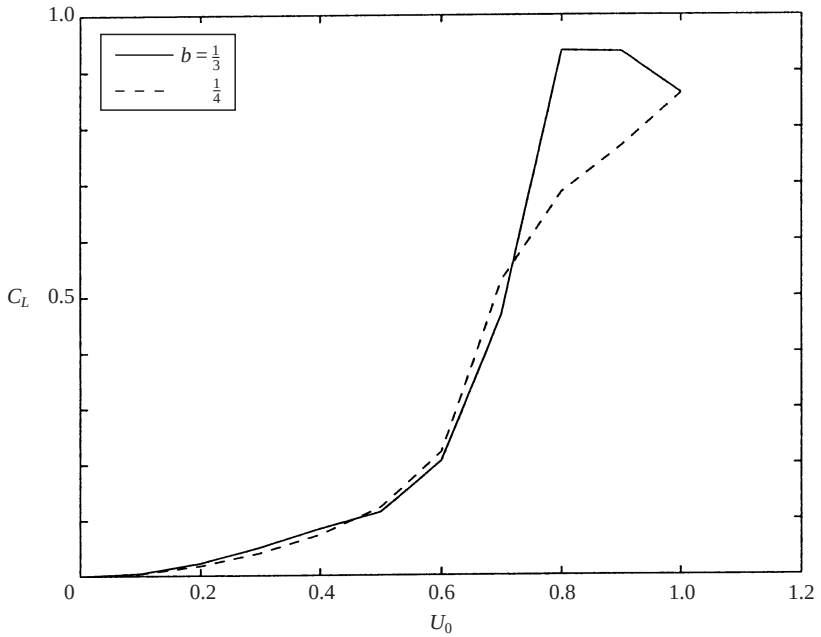

FIGURE 21. Coefficient of lift at $Re_j = 1000$ and $R = 2$.

shown in figure 21, it is found that the best measure of the control input for vectoring is the maximum suction velocity. The maximum average lift attained was similar for both cases, for the range of suction examined. However, for $b = \frac{1}{4}$, the 'hump', or the overshoot, that was observed in the C_L curve for the benchmark case is no longer present, consequently delaying the point of maximum lift. It is speculated that the

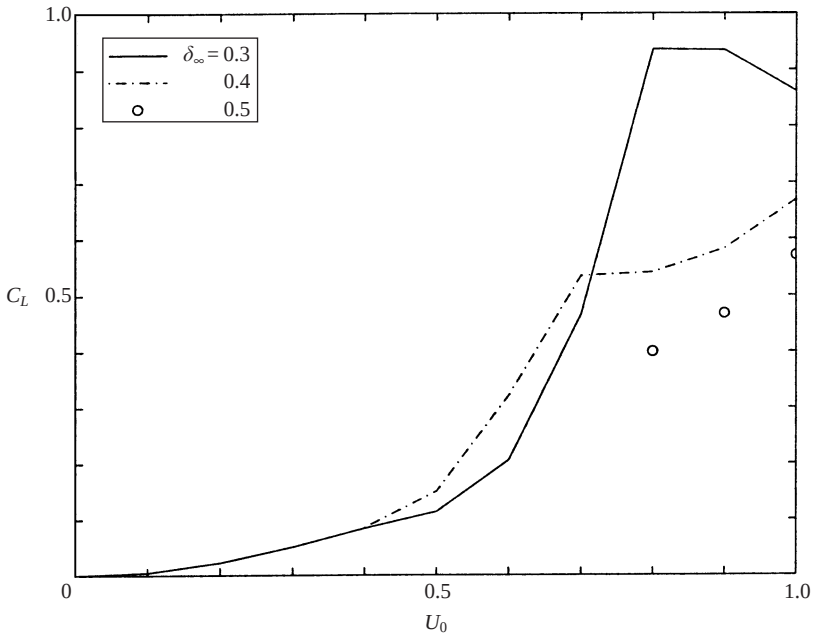

FIGURE 22. Coefficient of lift at $Re_j = 1500$, $R = 2$ and $b = \frac{1}{3}$.

disappearance of the overshoot may be related to the fact that decreasing b has a decoupling effect on the wake-shear layers.

4.3.4. *Effect of boundary-layer thickness*

Since the entrainment of the fluid from the boundary layers plays a crucial role in determining the tendency towards vectoring, it is natural to ask how the boundary-layer thickness would influence the lift patterns. Having observed that it is the boundary layers of the low-speed flow that are most affected by the asymmetric suction, two other values of δ_∞ were tested against the benchmark case of $\delta_\infty = 0.3$.

Figure 22 shows the time-averaged lift as a function of the suction flux ratio for $\delta = 0.3$, 0.4 and 0.5 at $Re_j = 1500$, $R = 2.0$ and $b = \frac{1}{3}$. The critical suction velocity remains essentially the same, and the main effect of increased boundary-layer thickness seems to be a marked decrease in the maximum lift produced. Indeed, it appears that the lift scales to the reciprocal of the boundary-layer thickness δ_∞, and this can be seen in figure 23 where the vectoring response is presented as the product $C_L\delta_\infty$. This pattern holds for the case of $b = \frac{1}{4}$ which is also shown on the same plot.

4.3.5. *Scaling problem*

The lift production by the use of asymmetric suction is very intuitive in one sense, and yet the actual mechanisms that contribute to lift for the configurations studied so far are not entirely clear. However, closer examination of results in figure 23 suggest that there is some dependence of the critical value of U_o on the velocity ratios, pointing to the fact that the vectored response probably depends on some combination of the velocity differences across the turning flows at the corners (i.e. $1 + U_o$ at the upper plate and $R + U_o$ at the lower plate). This point will only be clarified through further simulations covering a wider parametric variation of the co-flowing jet.

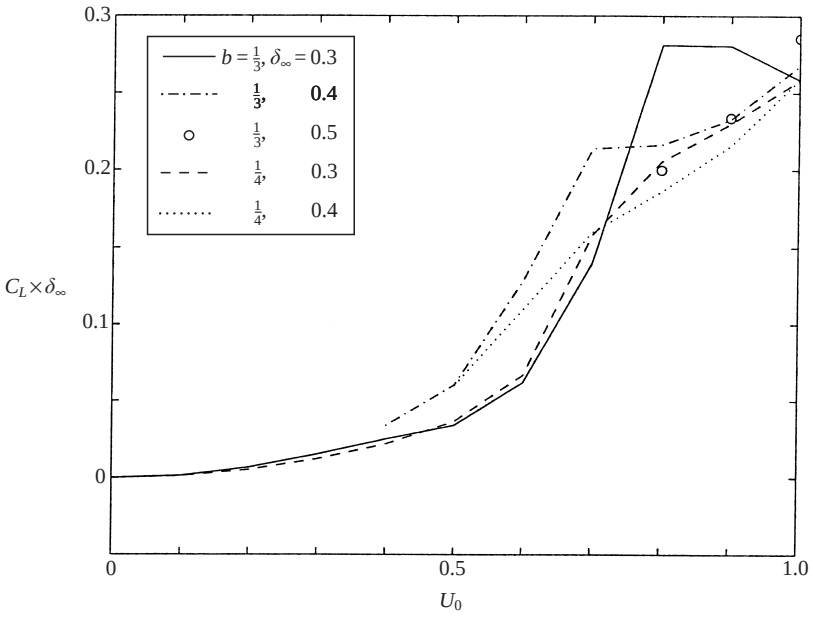

FIGURE 23. Coefficient of lift at $Re_j = 1500$ and $R = 2$.

4.4. *Jet spreading*

The entrainment patterns observed in the vectoring study suggest that base suction may provide an effective means for modifying the entrainment rates in the co-flowing jet. Mixing enhancement using annular suction in circular jets has been reported in the experimental work of Strykowski & Wilcoxon (1993). Their work provided laboratory evidence that sufficient counterflow around the jet induces global instability which, in turn, produces enhanced mixing. The results were interpreted in the framework of the transition to absolute instability in plane shear flows (e.g. Huerre & Monkewitz 1985), in particular that the region of absolute instability exceeded the critical value necessary for the onset of global instability with the application of suction. Strykowski *et al.* (1996*a*) further explored the mixing characteristics of compressible planar jets in a counterflowing configuration and showed that counterflow is effective in increasing the entrainment rates in the shear layers.

In the co-flowing jet configuration under study here, global instability is already present owing to the region of absolute instability in the near wakes of the trailing edges. However, based on the local entrainment patterns previously observed, it was anticipated that a symmetric suction profile with maximum suction velocity applied near the jet side of the lips may be used to 'pull' the jet apart and thereby enhance jet spreading. The following subsections describe the instability patterns and spreading characteristics resulting from this suction profile, which will be referred to as the 'symmetric' or 'spreading' profile in contrast to the 'asymmetric' or 'vectoring' profile used in the previous section. When distinction is helpful, the maximum suction velocity will be denoted by U_{0S} for the symmetric profile and U_{0A} for the asymmetric profile.

4.4.1. *Instability patterns for symmetric profile*

Figure 24 shows the temporal evolution of the streamwise velocity at $x = 3.0$ and $y = 0$ at two values of the peak suction velocity when the control parameters are set at $Re_j = 1500$, $R = 2.0$ and $b = \frac{1}{4}$. It is apparent that the range and magnitude

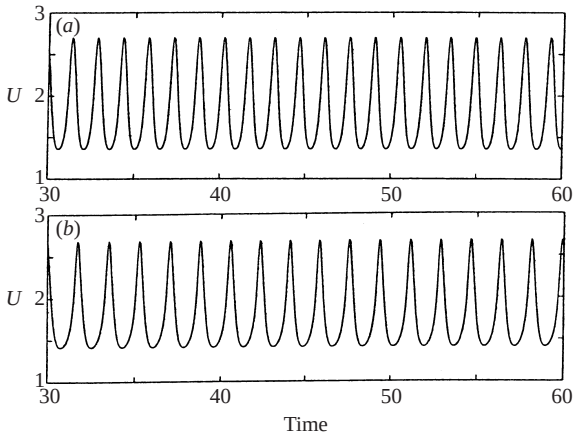

FIGURE 24. Time history of the streamwise velocity component at $x = 3.0$ and $y = 0$, for $Re_j = 1500$, $b = \frac{1}{4}$ and $R = 2$. (*a*) $U_{0S} = 0.2$; (*b*) $U_{0S} = 0.6$.

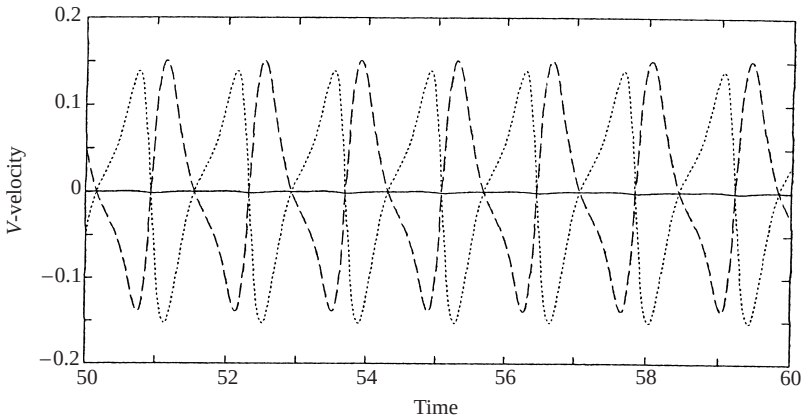

FIGURE 25. Time history of the cross-stream velocity component at $x = 3.0$, and at cross-stream positions on the centreline and half a cell position above and below the centreline. Velocity components at $Re_j = 1500$, $b = \frac{1}{4}$, $R = 2$ and $U_{0S} = 0$.

of the velocity fluctuation is nearly constant, but the frequency decreases, as the suction velocity is increased. The cross-stream velocity at the jet centreline remains essentially zero for the entire range of suction levels. The cross-stream velocity at a fixed streamline location at three grid points, on the centreline and half a cell dimension above and below the centreline, are shown in figure 25. It is clear that the instability is of varicose type.

As the peak suction velocity is increased further above 0.6, a transition is observed in the nature of the instability of the jet. At $U_{0S} = 0.65$, the amplitude of oscillations in the streamwise velocity starts to show a noticeable decay and the cross-stream velocity undergoes amplitude modulations, albeit infinitesimal, as shown in figure 26. This marks the critical suction level before the instability mode switches from varicose to sinuous type. Figure 27 shows the change that occurs as the suction velocity reaches $U_{0S} = 0.68$. The result was obtained by using a continuation method in which saturated results for $U_{0S} = 0.65$ are used as the initial condition, and demonstrates a sudden shift in the dynamics of the co-flowing jet as the suction velocity crosses

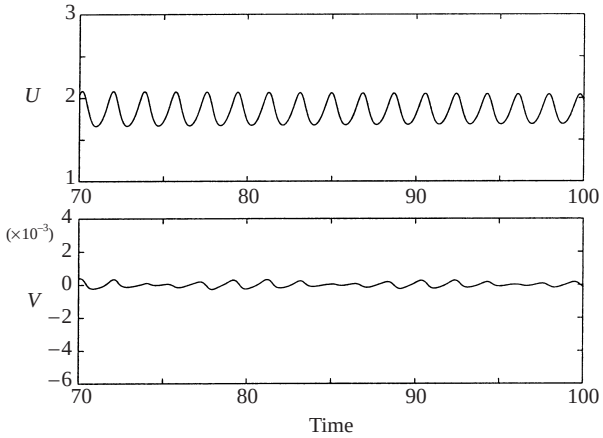

FIGURE 26. Time history of velocity components at $x = 3.0$ and $y = 0$, for $Re_j = 1500$, $b = \frac{1}{4}$, $R = 2$ and $U_{0S} = 0.65$.

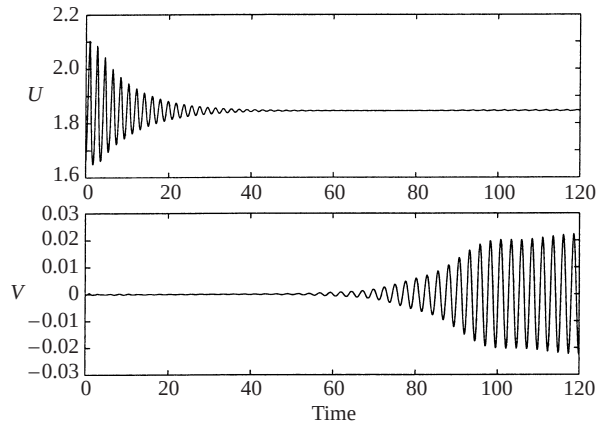

FIGURE 27. Time history of velocity components at $x = 3.0$ and $y = 0$, for $Re_j = 1500$, $b = \frac{1}{4}$, $R = 2$ and $U_{0S} = 0.68$.

the critical level. The amplitude of oscillations in the streamwise velocity at the jet centreline is dramatically reduced while the transverse velocity experiences significant oscillations, indicating the onset of the 'flapping' mode of the jet. Figure 28 shows traces of the velocity components at the same physical point in the flow field used in figures 24–26 for a supercritical suction level of $U_{0S} = 0.8$.

The variation of the frequency with increasing suction flux is shown in figure 29. There is a fairly abrupt decline in the Strouhal number when instability switches from the varicose mode to the sinuous mode. It should be noted that in the supercritical regime, there is also a subharmonic frequency which seems to be associated with the varicose mode. This is clearly visible in the streamwise velocity time histories along the centreline of the jet as shown in figure 28, but evidence of the subharmonic is quite weak away from the jet centreline.

4.4.2. *Spreading efficiency*

Several different measures were employed to evaluate the spreading efficiency of the co-flowing jet with and without suction. To begin, time-averaged streamwise velocity

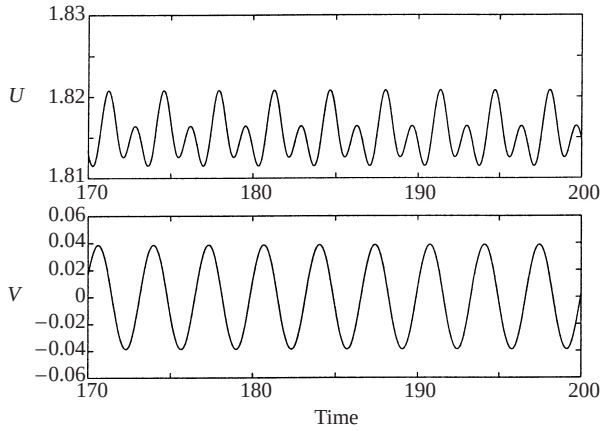

FIGURE 28. Time history of velocity components at $x = 3.0$ and $y = 0$, for $U_{0S} = 0.8$.

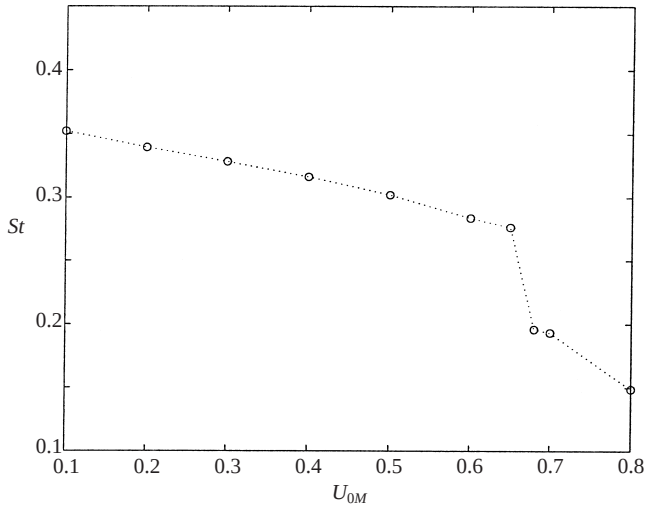

FIGURE 29. Variation of the dominant frequency with suction velocity U_{0S}, $Re_j = 1500$, $b = \frac{1}{4}$ and $R = 2.0$.

profiles were captured at various downstream locations in order to obtain a visual measure of the spreading rate of the shear layers. Figure 30 shows the time-averaged velocity profiles of the co-flowing jet at $Re_j = 1500$, $b = \frac{1}{4}$ and $R = 2$ at streamwise locations $x = 1.0$, 5.0, 8.0 and 10. In order to elucidate the effect of different instability modes on the mixing characteristics, three-way comparisons were made in the figure by including a subcritical suction case of $U_{0S} = 0.60$, a supercritical suction case of $U_{0S} = 0.8$, and the base case without suction. It was found that suction does indeed increase the spreading rate of the jet shear layers, but the effect is relatively small for subcritical suction when instability is of the same type as in the case of no suction (i.e. the varicose mode). When the suction is increased to $U_{0S} = 0.8$, however, the spreading rate is increased measurably at downstream distances of $x = 8.0$ and $x = 10$, as is evident in the bottom two subplots in figure 30. In fact, at $x = 10.0$ the shear layer width has increased to approximately twice the cross-stream extent for the case with no suction. Of course, the spreading portrayed here derives entirely from

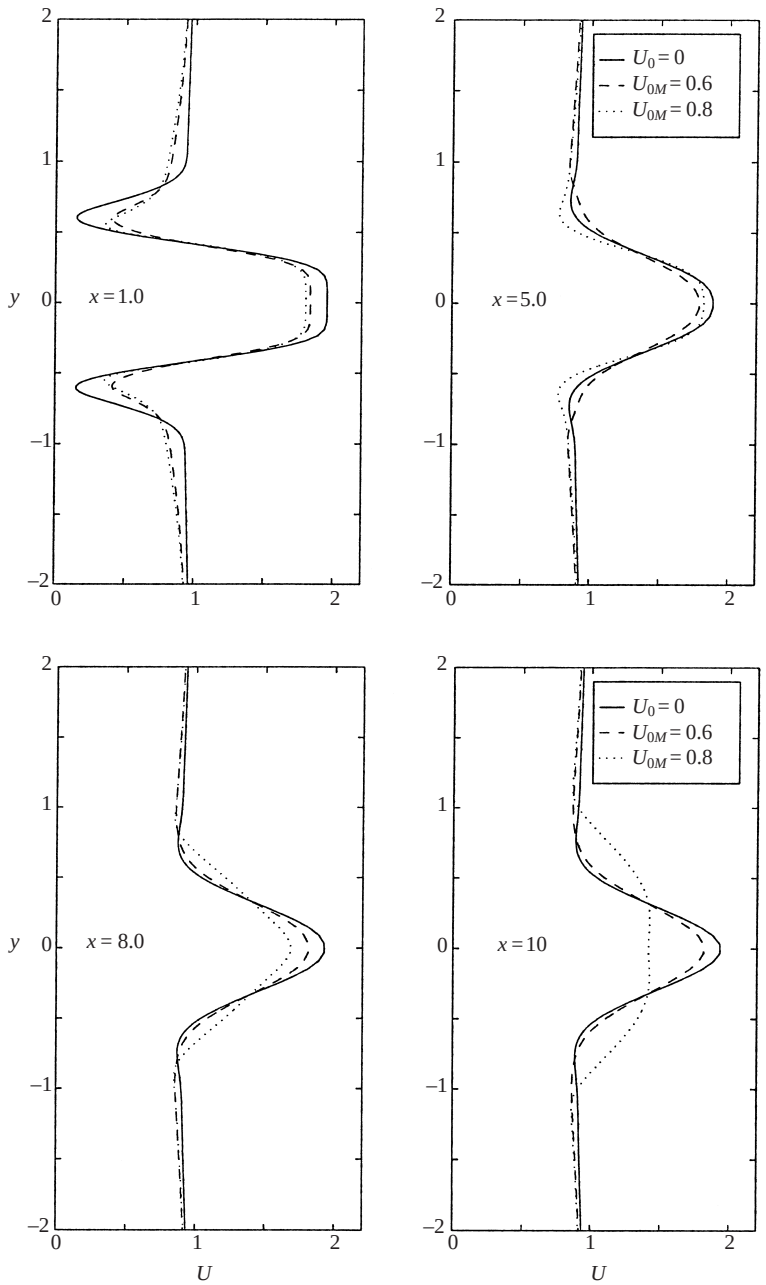

FIGURE 30. Time-averaged velocity profiles of the co-flowing jet with and without suction at various downstream locations for $Re_j = 1500$, $b = \frac{1}{4}$ and $R = 2$.

the increased flapping of the jet and should not necessarily be construed, especially for a two-dimensional simulation at low Reynolds numbers, as an increased entrainment by the jet.

Figure 31 shows the spatial variation of the time-averaged jet centreline velocity U_c, normalized by U_j, for $-1.0 \leqslant x \leqslant 12.0$. At a station twelve jet widths downstream from the jet exit, U_c decreased only about 4% from its inlet level when there was no

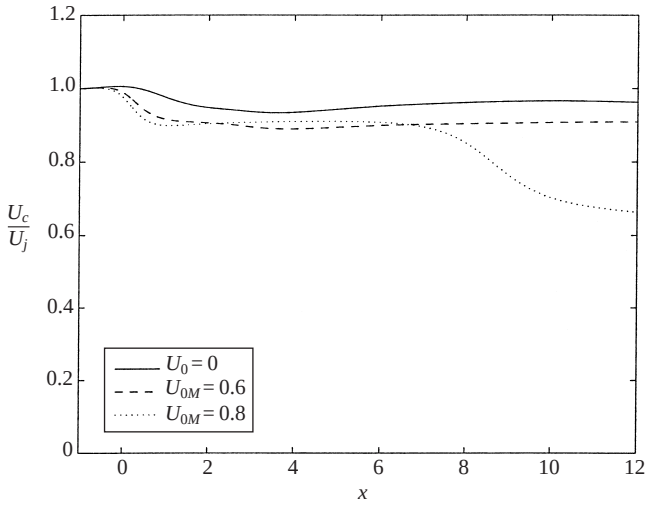

FIGURE 31. Spatial variation of time-averaged jet centreline velocity normalized by U_j, $Re_j = 1500$, $b = \frac{1}{4}$ and $R = 2$.

suction, and approximately 10% when $U_{0S} = 0.6$. It should be noted that these are very small levels of loss in comparison to free jets in which there are no co-flowing streams that 'compete' with the jet and effectively inhibit jet entrainment. The plot also reveals that the direct influence of suction, insofar as jet spreading is concerned, is limited to the first half jet width downstream ($0 \leqslant x \leqslant 0.5$) from the jet exit. However, its overall effect is greatly magnified when the instability is of sinuous type. As shown by the dotted curve in the same figure corresponding to the supercritical suction case of $U_{0S} = 0.8$, the decrease in the centreline velocity is similar to the subcritical suction case through the first seven jet widths downstream. However, between $x = 7.0$ and $x = 10.0$, the time-averaged jet centreline velocity is dramatically reduced so that the total decrease at $x = 12.0$ was about 33%. The difference is attributed to the flapping motion of the jet and suggests at least the potential for promoting mixing in the corresponding downstream region of the jet.

Another measure of the spreading characteristics of the flow is the local perturbation kinetic energy κ

$$\kappa = \tfrac{1}{2}\overline{(\hat{u}^2 + \hat{v}^2)},$$

where $\hat{u}$ and $\hat{v}$ represent the perturbations to the mean velocities (i.e. $U = \bar{U} + \hat{u}$ and $V = \bar{V} + \hat{v}$, where U and V are instantaneous solutions and the overbars indicate the corresponding time-averaged values). Figure 32 shows the perturbation kinetic energy profiles at four different downstream locations, presented in a manner similar to figure 30. The results appear somewhat puzzling at first since they reveal that the intensity of fluctuations is much stronger for the subcritical suction case in the near downstream region (both at $x = 1.0$ and $x = 5.0$). This is in apparent contradiction to what was observed for the time-averaged velocity profiles. However, the effect is a direct consequence of the strong streamwise oscillations present in the varicose mode instability at $U_0 = 0.6$ and, in contrast, the (relatively) weak oscillations in the streamwise velocity for the sinuous mode ($U_0 = 0.8$) in the same region. Whereas the dominant contribution to κ for the subcritical case comes from the streamwise fluctuations for the most part (as can be inferred from the peaks at $y = 0$ in figure 32

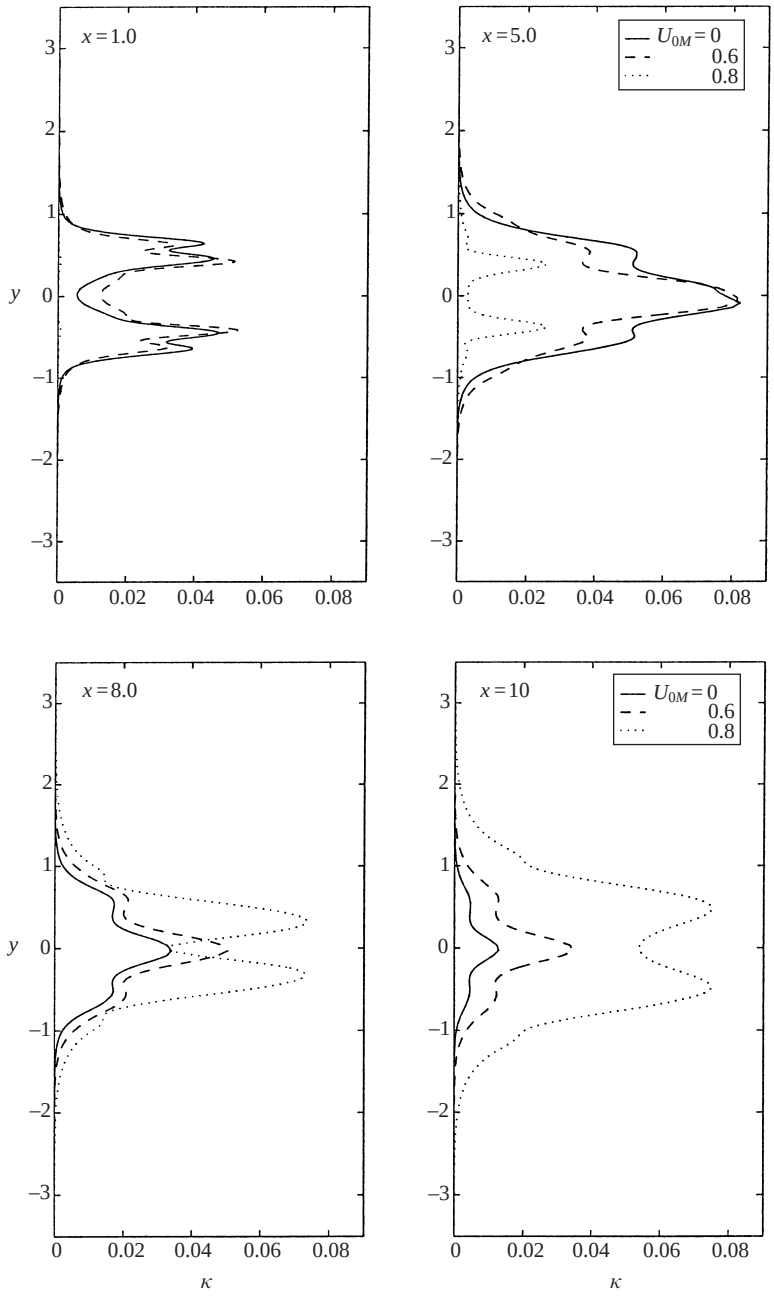

FIGURE 32. Perturbation kinetic energy profile at various streamwise locations for mixing profile, $Re_j = 1500$, $b = \frac{1}{4}$ and $R = 2$.

for $x = 5.0$ and beyond), it is the spatially growing cross-stream fluctuations in the sinuous mode oscillations that ultimately bring about greater spreading of the jet in the downstream region, as implied by the κ profiles at $x = 8.0$ and $x = 10.0$.

The stronger spreading evidenced in the case of the sinuous mode of instability raises the question of whether asymmetric suction profiles used in the vectoring study

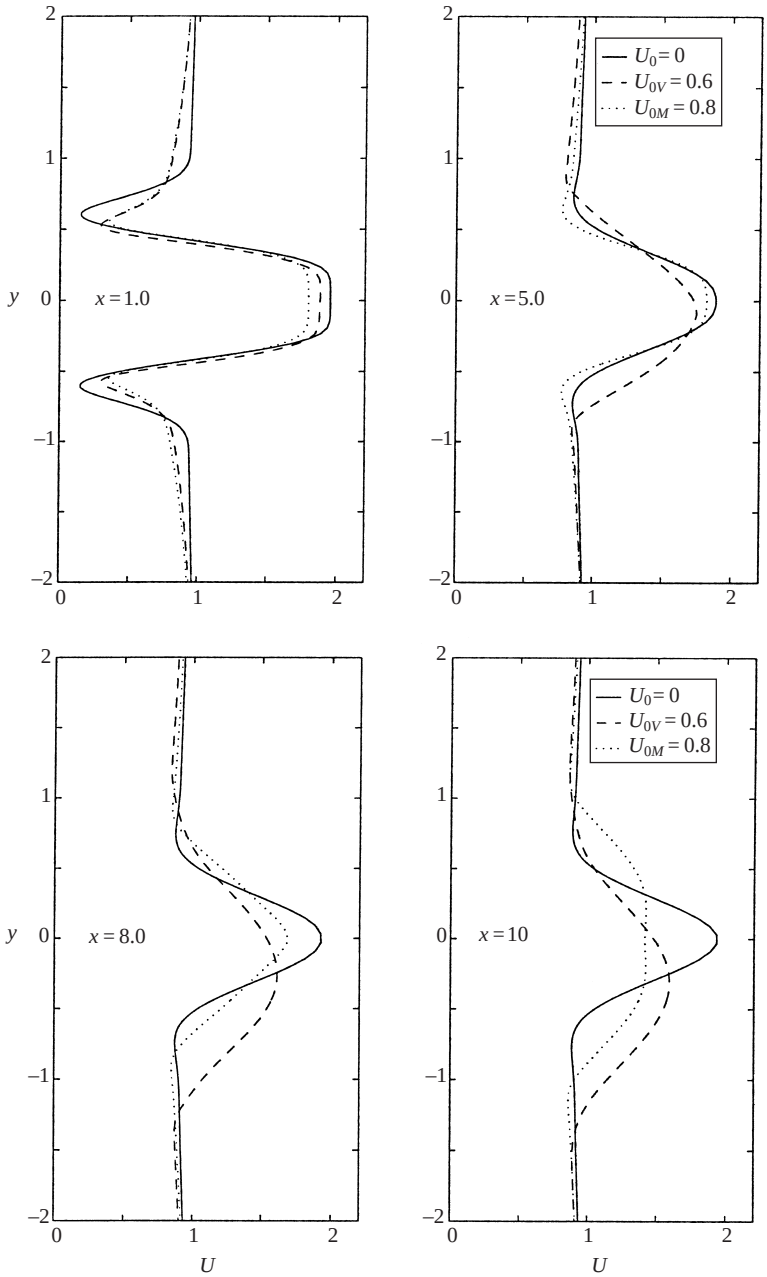

FIGURE 33. Time-averaged velocity profiles of the co-flowing jet with and without suction at various downstream locations for $Re_j = 1500$, $b = \frac{1}{4}$ and $R = 2$.

may be just as effective in enhancing the jet-spreading process, especially near the critical suction level when the flapping motion appeared most energetic. To consider this possibility, subcritical suction case of $U_{0A} = 0.6$ was chosen for asymmetric suction and was compared to the symmetric suction case of $U_{0S} = 0.8$. In both cases, the rest of the parameters were set at $Re_j = 1500$, $b = \frac{1}{4}$ and $R = 2.0$. Figure 33 shows the comparison of the time-averaged velocity profiles using the same scales as in

figure 30. It is evident that the asymmetric suction profile does quite well in spreading the jet profile, especially in the intermediate downstream regions between $x = 5.0$ and $x = 8.0$. The time-averaged jet centreline velocity in this interval is noticeably smaller than the corresponding value for the symmetric suction case. An important pointer emerging from these results is that spatially selective mixing enhancement may be possible through judicious distribution of base suction at the nozzle exit.

5. Concluding remarks

The results of the numerical simulations indicate that the application of distributed suction at the lips of a planar jet nozzle can provide an effective means of vectoring the jet in a co-flowing stream. It was found that there is a critical suction flux above which the jet experiences a fairly abrupt jump in the lift. Within the range of parameters studied, a maximum lift-to-thrust ratio of up to 17.5% was observed at a jet Reynolds number of 1800. It was shown that the critical suction flux q_{crit} (scaled to the jet volume flux) depended on the velocity ratio R, co-flow boundary-layer thickness δ_∞ and the relative plate thickness b, with values of q_{crit} ranging from 0.04 to 0.07. However, when the suction flux was scaled to the ambient flow using a dimensionless suction velocity U_0, the lift curves collapsed quite nicely, yielding a single critical number of approximately $U_0 = 0.7$. In general, increasing the jet Reynolds number increased the maximum lift-to-thrust ratio, while increasing either the velocity ratio R or the co-flow boundary-layer thickness δ_∞ had the opposite effect. We caution that the scaling relations revealed in this study for the vectored lift force are based on a somewhat limited range of the relevant parameters. Nevertheless, we believe that they are quite useful in that they provide a basis for estimating the performance of this approach to flow vectoring at other conditions.

Based on the results obtained thus far, it is possible to propose a simplified picture of the vectoring process. Vector plots of the type shown in figure 11 reveal that a corner flow appears around the jet lips at onset of vectoring. Before the critical suction flux is attained, vortices of alternate sign appear behind each lip and are shed into the downstream wake of each lip, subsequently merging into the jet shear layers. After the transition to vectoring, vortex shedding is (essentially) suppressed and a nearly stationary corner flow is established. The corner flow is most prominent behind the base and on the side of the jet lip where the suction velocity profile has a maximum. This suggests an interpretive picture of the flow field and an insight into the source of the associated lift force generated when the vortex shedding is marginally suppressed. Localized regions of concentrated vorticity of the same sign are formed in the regions of strong corner flow behind each lip when the asymmetric suction distribution corresponding to lifting configurations is enforced. Hence, a circulation-lift interpretation can be envisaged as sketched in figure 34.

Now, it seems reasonable to argue that the strength of these vortices should vary with the peak suction velocity for a given flow state (i.e. a given jet velocity ratio, etc.). The magnitude of the velocity difference across the vortex where the ambient flow is being vectored (i.e. the upper lip in figure 34) is $U_\infty + U_0$ while that on the opposite side is $U_j + U_0$. Hence, the strength of these vortices is dependent on the peak suction velocity U_0, a result which (perhaps) explains why the vectored lift is best scaled with U_0. This also suggests that the strongest vortex will appear behind the lip where the peak suction velocity is closest to the jet side of the lip. Although no simulations were performed using the production version of the code with the suction applied on only one side of the jet, some earlier validation tests support this conjecture. As

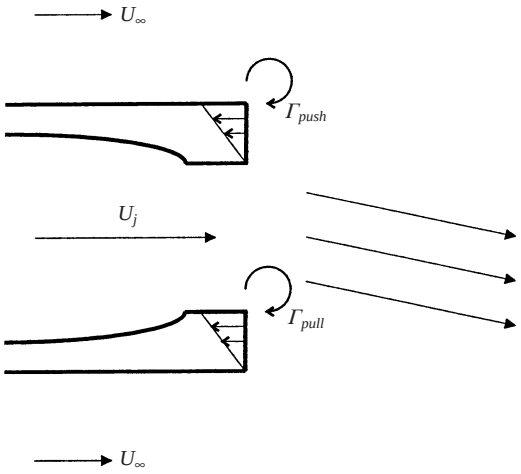

FIGURE 34. Circulation-lift concept for vectoring.

a consequence, the breaking of the symmetry of the jet flow through use of suction on only one side, the side where the jet is to be pulled toward the free stream, may be sufficient to achieve the dominant part of the vectoring force reported here. The pushing of the jet by vectoring the free stream toward the jet on the opposite side may contribute a much smaller reaction than that obtained from the pulling side. This is being explored in further studies aimed at clarifying the vectoring response to switch-on/off and harmonically pulsed suction. The pull *vs.* push aspects discussed here based on this simplified vortex picture are consistent with ideas put forward by Smith & Glezer (1998) in their study of the vectoring of jets exiting into a stationary background.

Symmetric suction distributions were shown to provide a substantial increase in the spreading of the two-dimensional jet in the downstream region ($x > 5.0$) once the suction velocity exceeded a critical level to induce the sinuous mode of jet instability. An energetic flapping motion of the jet was induced and was shown to have a far-reaching effect in determining the structure of the jet flow in the downstream region. The implications of this approach to the realization of significantly enhanced entrainment and small-scale mixing are beyond the reach of these two-dimensional, low-Reynolds-number simulations. Nevertheless, the present simulations do reveal that pronounced changes in the dynamics of the jet instability can be induced by the applied symmetric forcing and suggest that entrainment and mixing might be substantially altered in real flows as well.

In most technological applications, such as jet engines and combustion chambers, jet flows are subject to much higher velocities and temperatures. For a further study, therefore, it would be of considerable interest to examine the effects of compressibility and heating on the vectoring of a co-flowing jet. Strykowski *et al.* (1996*a*) carried out an experimental study on the vectoring of compressible, planar jets using a combination of suction and extension collars, as described in § 1. Encouraging results were obtained in their study.

Since the primary objective of the present study was to achieve thrust vectoring of a co-flowing jet by purely aerodynamic means, without the change or addition of physical boundaries, a future study that includes compressibility and temperature effects would give a more complete picture that is consistent with the present objective.

In general, studies exploring the onset of absolute instability in compressible flows have shown that an increase in the Mach number in the high-speed stream tends to reduce the absolute growth rate, making the flow more convectively unstable, whereas the effect of increased temperature has the opposite effect (see, for example, Monkewitz & Sohn 1988; Pavithran & Redekopp 1989; Yu & Monkewitz 1990; Yu & Monkewitz 1993). In particular, Yu & Monkewitz (1993) and Monkewitz *et al.* (1990) have shown experimentally that heating of the jet can induce a substantial increase in mixing via global instability in both planar and round jets. The competition between the opposing influences of increased Mach number and increased temperature, therefore, would provide an important underlying theme in evaluating the effectiveness of distributed suction in suppressing or enhancing the global mode and the subsequent vectoring or mixing enhancement in the co-flowing jet.

REFERENCES

Alvi, F. S. & Strykowski, P. J. 1999 Forward flight effects on counterflow thrust vector control of a supersonic jet. *AIAA J.* **37**, 179–181.

Alvi, F. S., Strykowski, P. J., Krothapalli, A. & Washington, D. 1996 Experimental study of a compressible countercurrent turbulent shear layer. *AIAA J.* **34**, 728–735.

Alvi, F. S., Strykowski, P. J., Krothapalli, A. & Forliti, D. J. 2000 Vectoring thrust in multiaxes using confined shear layers. *Trans ASME* I: *J. Fluids Engng* **122**, 3–13.

Ashley, S. 1995 Thrust vectoring: a new angle to air superiority. *Mech. Engng* pp. 58–64, Jan.

Buell, J. C. & Huerre, P. 1988 Inflow/outflow boundary conditions and global dynamics of spatial mixing layers. In *Proc. NASA Ames/Stanford Cent. Turbul. Res. Summer Program*, pp. 19–27.

Chorin, A. J. 1968 Numerical solution of the Navier–Stokes equations. *Math. Comput.* **22**, 745–762.

Davis, R. W. & Moore, E. F. 1982 A numerical study of vortex shedding from rectangles. *J. Fluid Mech.* **116**, 475–506.

Ferziger, J. H. & Perić, M. 1996 *Computational Methods for Fluid Dynamics*. Springer.

Hammond, D. A. & Redekopp, L. G. 1997*a* Global dynamics of symmetric and asymmetric wakes. *J. Fluid Mech.* **331**, 231–260.

Hammond, D. A. & Redekopp, L. G. 1997*b* Global dynamics and aerodynamic flow vectoring of wakes. *J. Fluid Mech.* **338**, 231–248.

Huerre, P. & Monkewitz, P. A. 1985 Absolute and convective instabilities in free shear layers. *J. Fluid Mech.* **159**, 151–168.

Leonard, B. P. 1979 A stable and accurate convective modelling procedure based on quadratic upstream interpolation. *Comput. Meth. Appl. Mech. Engng* **19**, 59–98.

Leu, T. S. & Ho, C. M. 2000 Control of global instability in a non parallel near wake. *J. Fluid Mech.* **404**, 345–378.

Maekawa, H., Mansour, N. N. & Buell, J. C. 1992 Instability mode interactions in a spatially developing plane wake. *J. Fluid Mech.* **235**, 223–254.

Monkewitz, P. A., Bechert, D. W., Barsikow, B. & Lehmann, B. 1990 Self-excited oscillations and mixing in a heated round jet. *J. Fluid Mech.* **213**, 611–639.

Monkewitz, P. A. & Sohn, K. D. 1988 Absolute instability in hot jets. *AIAA J.* **26**, 911–916.

Newman, B. G. 1961 The deflexion of plane jets by adjacent boundaries–Coanda effect. In *Boundary Layer and Flow Control* (ed. G. V. Lachmann), vol. 1, pp. 232–265. Pergamon.

North, D. M. 1994 MATV F-16 displays high alpha effects. *Aviat. Week. Space Tech.* pp. 42–45, 2 May.

Pauley, L. L., Moin, P. & Reynolds, W. C. 1990 The structure of two dimensional separation. *J. Fluid Mech.* **220**, 397–411.

Pavithran, S. & Redekopp, L. G. 1989 The absolute-convective transition in subsonic mixing layers. *Phys. Fluids* A **1**, 1736–1739.

Peyret, R. & Taylor, T. D. 1983 *Computational Methods for Fluid Flow*. Springer.

Proctor, P. 1995 Thrust vector control eyed for transports. *Aviat. Week. Space Tech.* pp. 45, 28 Aug.

Salvetti, M. V., Orlandi, P. & Verzicco, R. 1996 Numerical simulations of transitional axisymmetric coaxial jets. *AIAA J.* **34**, 736–743.

Smith, B. L. & Glezer, A. 1997 Vectoring and small scale motions effected in free shear flows using synthetic actuators. *AIAA J.* 97-0213, 35th Aerospace Sciences Mtg, Reno, NV, 6–10 Jan.

Smith, B. L. & Glezer, A. 1998 The formation and evolution of synthetic jets. *Phys. Fluids* **10**, 2281–2297.

Smith, B. L. 1999 Synthetic jets and their interactions with adjacent jets. PhD dissertation. Georgia Institute of Technology.

Strykowski, P. J., Krothapalli, A. & Forliti, D. I. 1996*a* Counterflow thrust vectoring of supersonic jets. *AIAA J.* **34**, 2306–2314.

Strykowski, P. J., Krothapalli, A. & Jendoubi, S. 1996*b* The effect of counterflow on the development of compressible shear layers. *J. Fluid Mech.* **308**, 63–96.

Strykowski, P. J. & Wilcoxon, R. K. 1993 Mixing enhancement due to global oscillations in jets with annular counterflow. *AIAA J.* **31**, 564–570.

Van der Veer, M. R. & Strykowski, P. J. 1997 Counterflow thrust vector control of subsonic jets: continuous and bistable regimes. *J. Propul. Power* **13**, 412–420.

Washington, D. M., Alvi, F. S., Strykowski, P. J. & Krothapalli, A. 1996 Multiaxis fluidic thrust vector control of a supersonic jet using counterflow. *AIAA J.* **34**, 1734–1736.

Yu, M. & Monkewitz, P. A. 1990 The effect of nonuniform density on the absolute instability of two-dimensional inertial jets and wakes. *Phys. Fluids* **2**, 1175–1181.

Yu, M. & Monkewitz, P. A. 1993 Oscillations in the near field of a heated two-dimensional jet. *J. Fluid Mech.* **225**, 323–347.